

# LD-ViCE: Latent Diffusion Model for Video Counterfactual Explanations

Payal Varshney<sup>1, 2\*</sup>, Adriano Lucieri<sup>1, 2</sup>, Christoph Balada<sup>1, 2</sup>, Sheraz Ahmed<sup>2</sup>, Andreas Dengel<sup>1, 2</sup>

<sup>1</sup>Rheinland-Pfälzische Technische Universität Kaiserslautern-Landau, Kaiserslautern, Germany

<sup>2</sup>German Research Center for Artificial Intelligence GmbH (DFKI), Kaiserslautern, Germany  
firstname.lastname@dfki.de

## Abstract

Video-based AI systems are increasingly adopted in safety-critical domains such as autonomous driving and healthcare. However, interpreting their decisions remains challenging due to the inherent spatiotemporal complexity of video data and the opacity of deep learning models. Existing explanation techniques often suffer from limited temporal coherence, insufficient robustness, and a lack of actionable causal insights. Current counterfactual explanation methods typically do not incorporate guidance from the target model, reducing semantic fidelity and practical utility. We introduce Latent Diffusion for Video Counterfactual Explanations (LD-ViCE), a novel framework designed to explain the behavior of video-based AI models. Compared to previous approaches, LD-ViCE reduces the computational costs of generating explanations by operating in latent space using a state-of-the-art diffusion model, while producing realistic and interpretable counterfactuals through an additional refinement step. Our experiments demonstrate the effectiveness of LD-ViCE across three diverse video datasets, including EchoNet-Dynamic (cardiac ultrasound), FERV39k (facial expression), and Something-Something V2 (action recognition). LD-ViCE outperforms a recent state-of-the-art method, achieving an increase in  $R^2$  score of up to 68% while reducing inference time by half. Qualitative analysis confirms that LD-ViCE generates semantically meaningful and temporally coherent explanations, offering valuable insights into the target model behavior. LD-ViCE represents a valuable step toward the trustworthy deployment of AI in safety-critical domains.

## Introduction

Video-based artificial intelligence (AI) systems are rapidly gaining prominence across high-stakes domains such as autonomous driving (Yurtsever et al. 2020), urban surveillance (Ullah et al. 2023), and clinical video diagnostics (Farhad et al. 2023). This growing adoption is supported by recent advances in large-scale spatiotemporal foundation models capable of processing minutes-long clips to produce temporally coherent predictions (Tang et al. 2025). Despite these advancements, video understanding remains significantly more challenging than static image recognition due to the intricate temporal dynamics, long-range dependencies, and causal interactions across frames. For instance, detecting suspicious behavior in surveillance footage

requires interpreting motion and intent over time, not just spatial patterns within individual frames (Arunnehru et al. 2023). This increased complexity means that errors in video-based predictions are difficult to diagnose and have far-reaching consequences in safety-critical settings. Misclassifications in medical ultrasound videos or missed anomalies in autonomous driving scenarios can lead to severe consequences. While explainability may not always prevent such failures, it is crucial for accountability and post-hoc analyses, offering insights into why specific decisions were made. Thus, explainable AI (XAI) is essential for fostering trust and regulatory compliance and supporting effective human oversight (Adadi and Berrada 2018). Despite these needs, explainability in the video domain remains substantially underexplored relative to the image domain.

Most existing explainability methods for video models adapt image-based techniques to the spatiotemporal domain. Feature attribution methods highlight regions influencing predictions (Stergiou et al. 2019; Li et al. 2021) but typically produce pixel-level saliency maps that lack semantic depth, temporal coherence, and robustness to noise (Adebayo et al. 2018; Arun et al. 2021). Concept-based methods link predictions to human-interpretable concepts (Ji, Wang, and Kato 2023; Saha et al. 2024), yet often rely on static clustering or predefined concept sets, limiting their ability to capture dynamic motion patterns critical for video understanding. While feature attribution reveals where a model attends and concept-based methods indicate what it focuses on, neither clarifies how the input must change to alter the prediction, making them non-actionable. For example, a saliency map may highlight an object and a concept-based explanation may confirm its relevance, but neither specifies whether the object should be added, removed, resized, or recolored to change the outcome. In contrast, counterfactual explanations (CEs) (Wachter, Mittelstadt, and Russell 2017) explicitly identify the minimal, targeted changes required to flip a model’s decision, offering actionable and causally grounded insights essential for video analysis.

Recently, generative approaches have been explored for producing video CEs. Existing methods (Reynaud et al. 2023; Zong et al. 2025) utilize diffusion models guided by textual prompts, without incorporating feedback from the target video model during generation. Instead, they follow a model-agnostic strategy, using the target model only for

\*Corresponding author. Email: payal.varshney@dfki.de

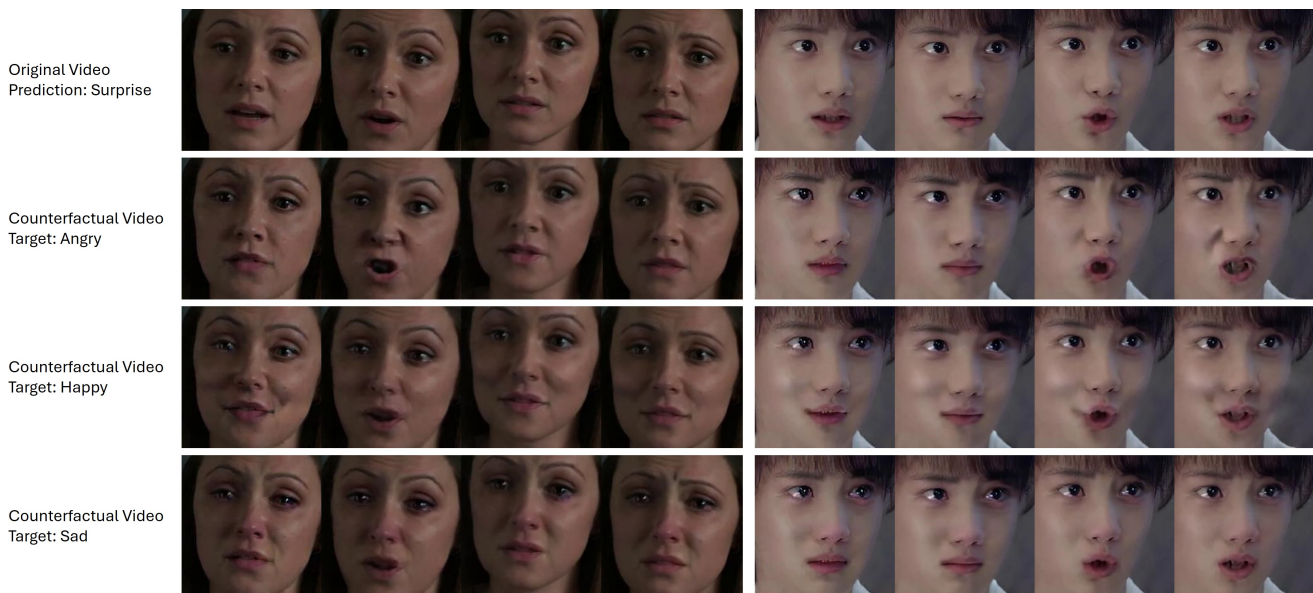


Figure 1: Qualitative counterfactual results generated by LD-ViCE on the FERV39k dataset. The generated counterfactuals exhibit distinct and class-consistent facial dynamics corresponding to the desired emotional categories. The first row shows four frames from two original videos predicted as *Surprise*. The second, third, and fourth rows display counterfactuals generated for the target emotion classes *Angry*, *Happy*, and *Sad*, respectively.

post-hoc evaluation rather than steering the generation process. Consequently, while these approaches can produce visually plausible counterfactuals, they offer limited insight into the model’s decision-making process. Moreover, both approaches operate entirely in pixel space, leading to high computational costs and poor scalability to longer sequences or higher-resolution videos.

To overcome these limitations, a novel method, Latent Diffusion for Video Counterfactual Explanations (LD-ViCE) is proposed, which generates counterfactual video explanations using a latent diffusion model guided explicitly by the target model. By operating in latent space, LD-ViCE significantly reduces computational cost while maintaining temporal coherence and visual fidelity. LD-ViCE integrates model feedback throughout generation, ensuring semantic and causal alignment with the model’s predictions. The main contributions of this paper are summarized as follows:

- To the best of our knowledge, LD-ViCE is the first latent diffusion-based framework for generating counterfactual video explanations with explicit target model guidance.
- LD-ViCE leverages SmoothGrad (Smilkov et al. 2017) to suppress noisy gradients and prevent adversarial artifacts during counterfactual optimization.
- A denoising refinement step is proposed within LD-ViCE to mitigate residual noise introduced by the diffusion denoising process, enhancing visual realism and stability.
- The effectiveness of LD-ViCE is demonstrated across diverse publicly available datasets, including EchoNet-Dynamic (cardiac ultrasound), FERV39k (facial expression recognition), and Something-Something V2 (action recognition).

## Related Work

Understanding the decision-making process of video models is essential due to their complex spatiotemporal architectures and increasing deployment in high-stakes applications. Explainability in the video domain remains far less developed than in the image domain, where post-hoc interpretability methods have advanced rapidly. Existing methods for explaining video-based models adapt techniques originally designed for 2D image classification, limiting their effectiveness for models that depend on rich temporal dynamics and higher-dimensional inputs (Hiley et al. 2020). Kolarik et al. (2023) provide a comprehensive survey of interpretability techniques in medical video analysis, underscoring their clinical relevance while highlighting critical gaps: the absence of standardized evaluation protocols and the limited temporal reasoning capabilities of current methods. This section discusses existing counterfactual video explanation methods and their key limitations.

Early works in counterfactual video explanation have focused on selecting existing evidence that flips a model’s prediction. Kanehira et al. (2019) present one of the earliest frameworks for generating multimodal explanations, identifying spatiotemporal tubes and corresponding attributes whose presence would alter the classifier’s decision. While insightful, the method is limited to masking or retrieving existing regions and cannot synthesize novel visual content, restricting its expressiveness in generating counterfactuals.

To move beyond region selection, generative methods have been explored to produce counterfactual video samples. Reynaud et al. (2022) leverage a conditional GAN to synthesize cardiac ultrasound videos conditioned on user-specified clinical factors, enabling actionable visual counter-

facts for model interpretation. However, the method inherits common GAN limitations, such as training instability, mode collapse, and reduced temporal consistency for longer sequences. More recently, diffusion models have emerged as a stable, higher-fidelity alternative for counterfactual video generation. Reynaud et al. (2023) propose a cascaded diffusion framework that generates high-resolution echocardiogram videos conditioned on clinical attributes and a randomly selected reference frame. This method processes only a single reference frame rather than the whole sequence, leading to poor temporal coherence, and it does not incorporate feedback from the target model. Similarly, Zong et al. (2025) introduce a multimodal debiasing pipeline using a text-guided diffusion model to generate fine-grained counterfactuals for video-based fake news detection. Although semantic control is achieved through textual prompts, the approach lacks supervision from the target classifier, reducing its explanatory power. In both cases, the target model is used only post-hoc for evaluation rather than guiding the counterfactual generation. Consequently, the resulting explanations may not reflect the model’s behavior or causal reasoning. Furthermore, both approaches operate in pixel space, incurring high computational cost and limiting scalability to longer or higher-resolution videos.

While classifier guidance has been explored in image-based counterfactual generation, it remains largely absent from video explanation methods (Jeanneret, Simon, and Jurie 2022; Augustin et al. 2022; Varshney et al. 2024). Notably, to the best of our knowledge, no prior work combines classifier-guided diffusion models with counterfactual generation for video explanations. To address this research gap, LD-ViCE is introduced, a framework for generating counterfactual video explanations via a latent diffusion process explicitly guided by the target model. By incorporating classifier feedback throughout generation, LD-ViCE ensures alignment with the model’s decision boundaries, while operating entirely in latent space preserves spatiotemporal coherence and significantly reduces computational cost compared to pixel-space approaches. This design enables scalable, causally valid, and temporally coherent counterfactual explanations for longer and higher-resolution videos.

## Methodology

We propose Latent Diffusion for Video Counterfactual Explanations (LD-ViCE), a novel framework for generating counterfactual video explanations, inspired by the image-based counterfactual generation process in CDCT (Varshney et al. 2024). In LD-ViCE counterfactual videos are generated using a text-to-video latent diffusion model with explicit guidance from a target model. Figure 2 illustrates the counterfactual generation pipeline of LD-ViCE.

### Problem Formulation

Let  $f_\phi : \mathcal{X} \rightarrow \mathcal{Y}$  be a pretrained target model to be explained that maps a video  $x \in \mathcal{X}$  to a class label or regression value  $y \in \mathcal{Y}$ . Given a factual video  $x_f \in \mathbb{R}^{F \times H \times W \times C}$  with  $F$

frames and model prediction  $y = f_\phi(x_f)$ , the objective is to generate a counterfactual video  $x_{cf} \in \mathbb{R}^{F \times H \times W \times C}$  with target  $y'$  that is visually plausible and semantically minimal, satisfying

$$f_\phi(x_{cf}) = y', \quad \text{where } y' \in \mathcal{Y}, y' \neq y.$$

Among all plausible alternatives,  $x_{cf}$  should represent the minimal set of changes needed to alter the model’s decision, while preserving spatiotemporal coherence. To achieve this, the generation process is guided along trajectories aligned with the decision boundary of  $f_\phi$ , using classifier gradients to ensure that modifications are sparse and causally relevant.

### Latent Diffusion-Based Video Counterfactual Generation

LD-ViCE produces counterfactual explanations for video models ranging from lightweight networks to transformer-based architectures, and is also task-agnostic, generalizing effectively across tasks such as regression and classification. In contrast to prior work (Reynaud et al. 2023), LD-ViCE leverages a text-to-video latent diffusion model (LDM), whose operation in a compressed latent space enables significantly lower computational cost, faster sampling, and reduced memory usage, while still generating high-quality, temporally coherent counterfactual videos.

**Forward Diffusion Process** The factual video  $x_f$  is transformed to a spatiotemporal latent representation by the encoder  $\mathcal{E}$  of the text-to-video latent diffusion model. This latent preserves spatial detail and motion consistency while enabling efficient processing. The encoded video is then perturbed using the forward diffusion process defined by a variance schedule  $\beta_t \in (0, 1)$ , with the cumulative product:

$$\bar{\alpha}_t = \prod_{k=1}^t (1 - \beta_k), \quad 1 \leq t \leq T$$

The noisy latent at step  $T$  is obtained as:

$$z_T = \sqrt{\bar{\alpha}_T} \cdot \mathcal{E}(x_f) + \sqrt{1 - \bar{\alpha}_T} \cdot \epsilon_T, \quad \epsilon_T \sim \mathcal{N}(0, I)$$

Simultaneously, a text prompt  $c$ , incorporating the counterfactual class label  $y'$  in textual form and relevant metadata, is encoded via the text encoder  $\tau_\delta(c)$ .

**Reverse Diffusion Process with Causal Guidance** The reverse denoising process  $z_T \rightarrow z_0$  is guided by the gradients of the target task. The following steps are performed at each denoising step  $t = T, \dots, 1$ :

- The diffusion denoising model  $\epsilon_\theta$  predicts the noise component  $\hat{\epsilon}_t$ :

$$\hat{\epsilon}_t = \epsilon_\theta(z_t, \tau_\delta(c), t)$$

- DDIM sampling (Song, Meng, and Ermon 2020)  $\mathcal{S}$  estimates the previous noisy latent  $\tilde{z}_{t-1}$  and the clean latent  $v_t$ :

$$\tilde{z}_{t-1}, v_t = \mathcal{S}(z_t, \hat{\epsilon}_t, t)$$

- The estimated clean latent  $v_t$  is decoded into the video:

$$\tilde{x}_t = D(v_t)$$

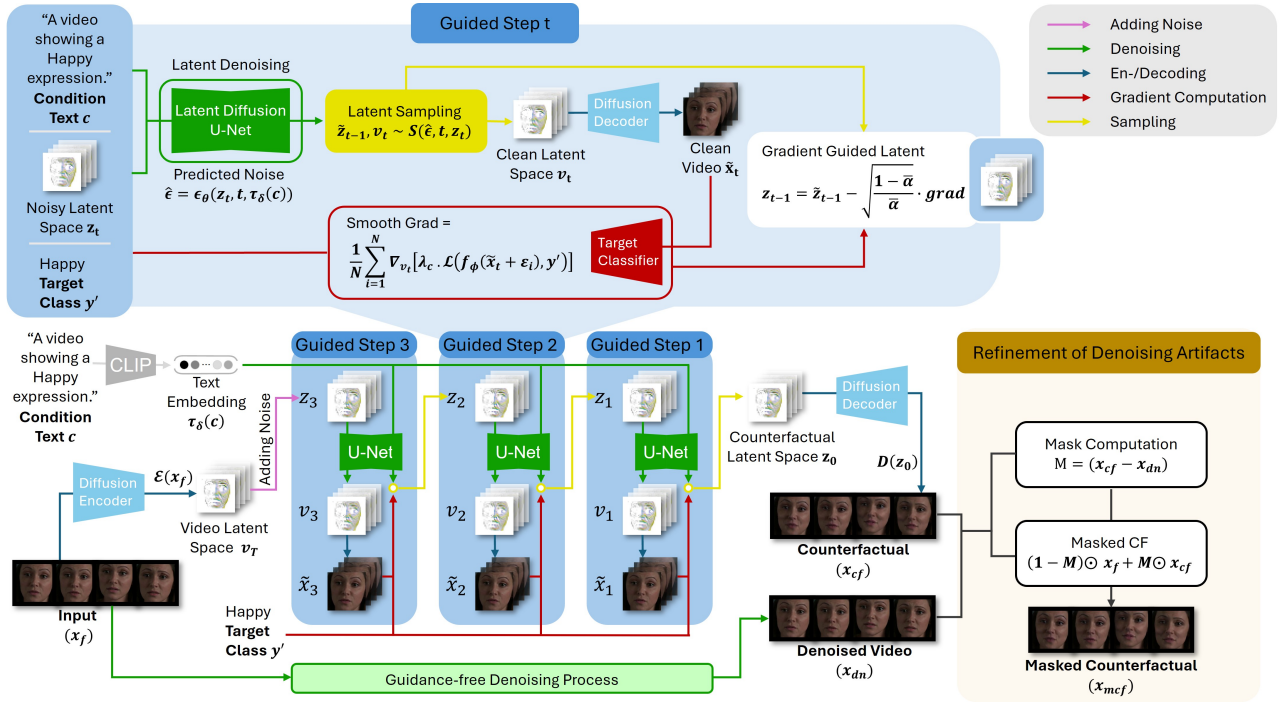


Figure 2: Overview of the LD-ViCE counterfactual generation process. The factual video  $x_f$  is encoded and perturbed to obtain the noisy latent  $z_T$  (here,  $T = 3$ ), while the conditional text prompt  $c$  is embedded via the text encoder  $\tau_\delta(c)$ . At each guided denoising step  $t$ , the latent  $z_t$  and embedding  $\tau_\delta(c)$  are provided to the diffusion model. The U-Net predicts the noise  $\hat{\epsilon}$ , which is used in the sampling process to compute the clean latent  $v_t$  and the less noisy latent  $\tilde{z}_{t-1}$ . The clean latent  $v_t$  is decoded to produce  $\tilde{x}_t$ , which is used to estimate SmoothGrad-based classifier gradients, scaled by  $\lambda_c$ , to compute the updated latent  $z_{t-1}$ . After the final step,  $z_0$  is decoded into the counterfactual video  $x_{cf}$ . A refinement stage follows, where the same  $z_T$  is denoised without guidance to obtain a clean reference video, which is used to compute a mask for reducing diffusion artifacts in  $x_{cf}$ .

- The target model  $f_\phi$  is applied to compute the task specific loss  $\mathcal{L}$  with respect to the target value  $y'$  and the gradient is scaled by  $\lambda_c$  as :

$$\nabla_{v_t} \mathcal{L}_{CE} = \nabla_{v_t} [\lambda_c \cdot \mathcal{L}(f_\phi(\tilde{x}_t), y')]$$

- The noisy latent is updated using the gradient:

$$z_{t-1} = \tilde{z}_{t-1} - \sqrt{\frac{1 - \bar{\alpha}_t}{\bar{\alpha}_t}} \cdot \nabla_{v_t} \mathcal{L}_{CE}$$

The updated latent  $z_{t-1}$  is input for the next reverse step. After  $T$  reverse steps,  $z_0$  is obtained, which is decoded by the decoder  $D$  to produce the counterfactual video:

$$x_{cf} = D(z_0)$$

Similar to the previous method by Farid et al. (2023), LD-ViCE leverages DDIM sampling (Song, Meng, and Ermon 2020) that analytically computes and returns the clean latent representation at every diffusion timestep. The computational complexity is  $\mathcal{O}(T)$ , enabling efficient inference while preserving high-quality counterfactual generation.

### Smooth Gradient for Robust Guidance

Relying on raw gradients for guidance in counterfactual generation can introduce noise, instability, and adversarial artifacts into the explanations. To ensure semantic coherence,

guidance must be smooth and resilient to small input perturbations, producing counterfactuals that capture consistent, meaningful changes rather than spurious artifacts. SmoothGrad (Smilkov et al. 2017) based gradient estimation is applied to mitigate these issues. SmoothGrad averages gradients over multiple perturbed inputs to suppress spurious variations, resulting in smoother guidance. It leads to more stable and visually coherent counterfactuals, thereby improving the interpretability of the explanation. Formally, the SmoothGrad-guided gradient at timestep  $t$  for the latent representation  $v_t$  is computed as:

$$\nabla_{v_t} \mathcal{L}_{CE} = \frac{1}{N} \sum_{i=1}^N \nabla_{v_t} [\lambda_c \cdot \mathcal{L}(f_\phi(\tilde{x}_t + \epsilon_i), y')],$$

$$\epsilon_i \sim \mathcal{N}(0, \sigma^2 I)$$

Here,  $N$  represents the number of noise perturbations, and  $\sigma$  controls the smoothness of the gradient estimation. SmoothGrad enhances robustness to input noise, suppresses spurious gradients to highlight semantically meaningful regions, and prevents overfitting to model irregularities.

### Refinement of Denoising Artifacts

The diffusion denoising process introduces visual artefacts that reduce counterfactual fidelity. To isolate causally rele-

vant changes, the same latent  $z_T$  is denoised without guidance to produce a clean reference  $x_{\text{den}}$ . Despite the stochastic nature of diffusion, a fixed seed and deterministic scheduler ensure structural alignment with the guided output. A threshold-based mask filters out small, noise-induced differences, allowing the suppression of artifacts from the diffusion process and gradient guidance while preserving meaningful changes.

A binary refinement mask  $M \in \{0, 1\}^{F \times H \times W}$  is computed by comparing the counterfactual video  $x_{\text{cf}}$  with the denoised reconstruction of the original  $x_{\text{den}}$ :

$$\Delta(f, h, w) = \sum_{c=1}^3 |x_{\text{cf}}(f, h, w, c) - x_{\text{den}}(f, h, w, c)|$$

$$M(f, h, w) = \mathbb{I}[\Delta(f, h, w) > t_{\text{sup}}]$$

where  $\mathbb{I}[\cdot]$  is the indicator function, and  $t_{\text{sup}}$  is a scalar threshold chosen empirically. The binary mask  $M$  is broadcast along the channel axis to form the refined counterfactual:

$$x_{\text{mask.cf}} = (1 - M) \odot x_{\text{f}} + M \odot x_{\text{cf}}$$

where  $\odot$  denotes element-wise multiplication. This formulation replaces only those voxels flagged by  $M$ , thereby retaining the original content elsewhere and suppressing residual artefacts.

## Experiments & Results

This section describes the experimental setup and presents a comprehensive evaluation of the proposed LD-ViCE framework.

### Datasets and Target Models

LD-ViCE is evaluated on three benchmark datasets spanning diverse video domains. A state-of-the-art network is used as a black-box target model for each dataset, without modifying its parameters.

**FERV39K** A facial expression recognition dataset (Wang et al. 2022) with seven emotion categories (multiclass classification). The publicly available Static-to-Dynamic (S2D) model (Chen et al. 2024) is utilized as the black-box target. This architecture extends a Vision Transformer by incorporating Temporal Modeling Adapters to adapt image features dynamically across time.

**EchoNet-Dynamics** An echocardiography video dataset (Ouyang et al. 2020) annotated with continuous left-ventricular ejection-fraction (LVEF) values (regression task). The 3D ResNet variant leveraged by EchoDiffusion (Reynaud et al. 2023) is trained using the provided configuration and adopted as the black-box regressor, since pretrained weights are not publicly available.

**Something-Something V2 (SSv2)** A fine-grained human-action dataset (Goyal et al. 2017) with 174 classes (multiclass classification). The publicly released VideoMAE-Base model (Tong et al. 2022) served as the black-box

classifier. It is a spatio-temporal Vision Transformer pre-trained by masked autoencoding and equipped with factorised space-time attention.

### Fine-tuning of Diffusion Model

The text-to-video diffusion model, CogVideoX (Yang et al. 2024)<sup>1</sup>, is fine-tuned independently on each dataset. Frame sampling and input dimensions are aligned with the input requirements of the corresponding target model, with 16 frames extracted per video at a sampling rate of 8 frames per second. Training captions are generated for each video by incorporating ground truth class labels or regression values and available metadata. These captions enrich the conditioning signal during fine-tuning. The CogVideoX model is fine-tuned on each dataset for 50 epochs with a learning rate of  $1e - 3$ , enabling the generation of realistic samples.

### Video Counterfactual Generation

The proposed LD-ViCE framework generates counterfactual videos across all datasets. Three variants are evaluated: (i) Raw Gradient guidance (RG), (ii) SmoothGrad-based guidance (SG), and (iii) SmoothGrad combined with denoising Artifact suppression (SGA). Counterfactual generation in LD-ViCE is controlled by three key hyperparameters: the gradient loss scale ( $\lambda_c$ ), the number of denoising inference steps ( $T$ ), and the artifact suppression threshold ( $t_{\text{sup}}$ ). Ablation studies were first conducted to select optimal values for  $\lambda_c$  and  $T$  using the SmoothGrad variant. Based on these selected values, the optimal threshold for artifact suppression was determined for the SGA variant. The raw gradient variant (RG) was evaluated using the same  $\lambda_c$  and  $T$  settings for consistency. A comparative analysis of three variants and ablation studies for selecting hyperparameter values is provided in the Appendix.

**Regression Results** Figure 3 compares counterfactuals from LD-ViCE variants and the baseline (Reynaud et al. 2023) on the EchoNet-Dynamics dataset for LVEF prediction. The baseline (Reynaud et al. 2023) predicts an LVEF of 45.1, well above the target, likely reflecting its reliance on a single frame and target text without incorporating model feedback, which may limit temporal consistency. In contrast, LD-ViCE processes the whole video with gradient guidance, producing temporally coherent counterfactuals with tighter alignment to the target value. Among the variants, SG yields predictions closest to the target, whereas SGA achieves higher perceptual quality but deviates more from the target. This deviation may result from retaining subtle variations from the original video, including details that are not directly relevant to LVEF prediction.

Table 1 reports regression accuracy ( $R^2$ , MAE, RMSE), structural similarity (SSIM), perceptual quality (LPIPS), and inference time (per counterfactual video on an NVIDIA A100 GPU, excluding model loading). Reynaud et al. (2023) generate three independent counterfactuals per input and report both the average and the best-performing sample. Since

<sup>1</sup>Fine-tuning code adapted from <https://github.com/huggingface/diffusers/tree/main/examples/cogvideo>.

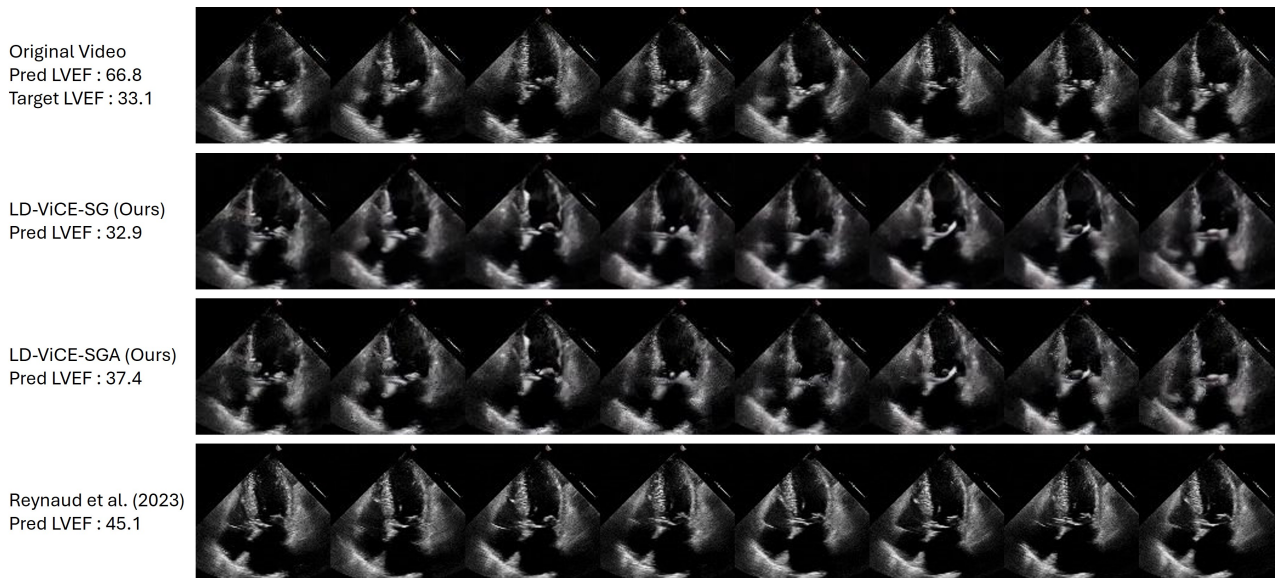


Figure 3: Qualitative comparison of counterfactual explanations on the EchoNet-Dynamics dataset, demonstrating LD-ViCE’s improved alignment between counterfactual explanations and target regression values. The first row displays eight frames from the original video, while the following rows show counterfactuals generated using LD-ViCE-SG, LD-ViCE-SGA, and EchoDiffusion (Reynaud et al. 2023), respectively. The predicted and target LVEF values are given on the left.

the target model is trained on 16 frames, comparisons are limited to the 1SCM variant of their method. For fairness, metrics for (Reynaud et al. 2023) were recomputed, as their approach uses a random target value, whereas this study derives the target from the predicted value. All LD-ViCE variants surpass the average and best baseline results of the previous state of the art across various metrics. SG offers the best trade-off between target fidelity and visual quality, combining low prediction error with strong perceptual realism. RG achieves slightly lower MAE but with reduced visual quality (higher LPIPS), while SGA yields the most realistic counterfactuals (highest SSIM, lowest LPIPS) with a slight reduction in regression accuracy. All variants run significantly faster than the method by Reynaud et al. (2023), underscoring the efficiency of the proposed framework. These results confirm that LD-ViCE generates visually coherent and semantically aligned counterfactuals with the intended regression targets, advancing the state of the art in counterfactual video explanations for medical imaging.

**Classification Results** Counterfactual results for the FERV39K dataset are discussed below, and results for the Something-Something V2 dataset are presented in the Appendix. Figure 1 illustrates counterfactual video explanations generated by LD-ViCE on the FERV39K dataset. The videos reflect plausible spatiotemporal transformations in facial expressions corresponding to the target classes. For instance, counterfactual videos targeting anger exhibit furrowed brows, tightened lips, and pronounced tension in the eye region. In videos targeting sadness, subtle cues such as redness around the eyes and nose, gentle downward shifts in the mouth corners, and slight chin muscle contraction emerge consistently. Conversely, the happy counterfactuals

Method	Time ↓	$R^2$ ↑	MAE ↓	RMSE ↓	SSIM ↑	LPIPS ↓
R23	42 s	0.31	7.89	9.74	0.52	0.22
R23*	126 s	0.71	4.68	6.31	0.53	0.21
RG	<b>6 s</b>	<b>0.99</b>	<b>0.49</b>	1.24	0.75	0.19
SG	23 s	<b>0.99</b>	0.50	<b>1.02</b>	0.75	0.17
SGA	24 s	0.90	2.78	3.75	<b>0.84</b>	<b>0.13</b>

Table 1: Quantitative comparison of regression accuracy, visual quality, and inference time for counterfactuals generated by LD-ViCE variants (RG, SG, SGA) and the baseline 1SCM model from Reynaud et al. (2023) (R23=average, R23\*=best), evaluated on the EchoNet-Dynamic validation split (1,288 videos). Best values are highlighted in bold. LD-ViCE outperforms the baselines across all metrics while achieving substantially faster inference.

prominently show upward curvature of the mouth, cheek elevation, and softening of the eye region, reflecting typical positive affective expressions. Changes in mouth movement, eye expression, and brow position are semantically aligned with the intended emotions, indicating that LD-ViCE produces class-discriminative yet realistic counterfactuals.

Table 2 presents quantitative results for counterfactuals generated by the LD-ViCE variants on the FERV39K dataset. The flip ratio (FR) is high for all variants, indicating that most generated counterfactuals are classified as the intended target class. The RG and SG variants achieve the highest FR while maintaining visual quality, with SG achieving the best FID and FVD scores. The SGA variant, although exhibiting a lower FR, yields the highest structural similarity (SSIM) and the lowest perceptual distance

Method	FR $\uparrow$	SSIM $\uparrow$	LPIPS $\downarrow$	FID $\downarrow$	FVD $\downarrow$
RG	<b>0.986</b>	0.845	0.167	4.152	31.097
SG	0.984	0.846	0.165	<b>4.081</b>	<b>29.242</b>
SGA	0.814	<b>0.934</b>	<b>0.127</b>	9.089	35.727

Table 2: Quantitative comparison of counterfactuals generated by LD-ViCE variants (RG, SG, and SGA), evaluated on the FERV39K dataset test split (7847 videos). Best values are highlighted in bold. Results illustrate a trade-off between classification effectiveness (FR) and perceptual quality (SSIM, LPIPS) among the variants.

(LPIPS), indicating its strength in preserving visual fidelity through localized, artifact-free modifications. These results highlight the trade-off between classification success and perceptual quality across the variants.

Figure 4 illustrates counterfactuals generated by different LD-ViCE variants for all target classes in the FERV39K dataset, showing the same frame from each counterfactual video. The difference maps are obtained by subtracting the factual frame from the corresponding counterfactual frame. Across all target emotions, the SG variant produces counterfactuals emphasizing key facial regions such as the brows, eyes, cheeks, and mouth, as evident in the corresponding difference maps. However, these maps also show widespread changes across the entire video frame, including minor activations in irrelevant areas such as the microphone region. The diffusion denoising process may induce these minor changes and should be refined to produce more meaningful counterfactuals. As seen in the corresponding difference maps, the SGA variant mitigates such artifacts, yielding more spatially localized modifications concentrated in expression-critical regions. These localized modifications align closely with semantically relevant facial cues, indicating improved focus and reduced background interference compared to the SG variant. These results underscore the explanatory power of the LD-ViCE generated counterfactuals, providing actionable insights into black-box model behavior consistent with human intuition and expert domain knowledge.

### Limitations & Future work

While LD-ViCE demonstrates strong performance across diverse tasks, some aspects require further investigation to improve reliability and interpretability. Existing frame-wise metrics (e.g., LPIPS, SSIM) do not capture temporal coherence, highlighting the need for dedicated video-specific evaluation measures. Although the artifact suppression module improves visual fidelity and counterfactual alignment, it can reduce task-specific predictive accuracy. This trade-off highlights the importance of developing principled approaches to disentangle causal effects from reconstruction-induced variations. Expert validation, especially in high-stakes domains like medical imaging, remains essential to ensure explanations’ clinical plausibility and trustworthiness. Additionally, while concepts within counterfactual explanations are generally intuitive when aligned with human-

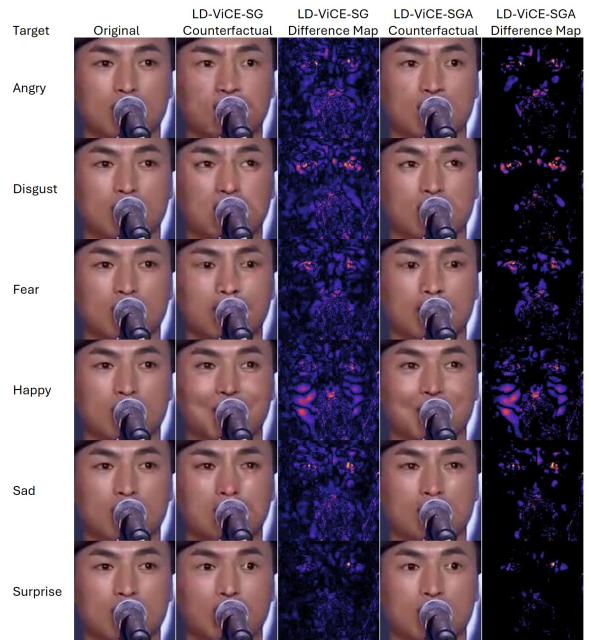


Figure 4: Qualitative comparison of counterfactuals generated by LD-ViCE variants on the FERV39k dataset. LD-ViCE-SGA variant focuses on expression-relevant facial regions. Each row shows a frame from the original video, the corresponding counterfactual from the LD-ViCE-SG and LD-ViCE-SGA variant, with its corresponding difference map. Target emotions are shown in the leftmost column.

recognizable features, they become more challenging to interpret when counterfactuals reveal novel or unfamiliar semantic patterns. Future work should develop automated methods to extract and interpret such concepts, improving reliability and practical utility.

### Conclusion

As deep learning advances in video understanding tasks, the need for explainable methods has become increasingly critical, especially in safety-sensitive domains such as healthcare and surveillance. Counterfactual explanations offer a powerful means of interpreting model behavior by revealing causal relationships along temporal decision boundaries. We introduce LD-ViCE, a novel framework for generating counterfactual video explanations using a latent diffusion model. By operating in latent space and integrating gradient-based guidance, LD-ViCE produces temporally coherent, visually plausible counterfactuals at a lower computational cost than pixel-space approaches. A masking-based artifact suppression module refines outputs by isolating causal edits while minimizing modifications in non-causal regions. Comprehensive experiments on diverse tasks show consistent improvements over state-of-the-art baselines. Collectively, these findings establish LD-ViCE as a robust and versatile paradigm for producing high-fidelity, temporally consistent, and interpretable video explanations across various applications.

## References

- Adadi, A.; and Berrada, M. 2018. Peeking inside the black-box: a survey on explainable artificial intelligence (XAI). *IEEE access*, 6: 52138–52160.
- Adebayo, J.; Gilmer, J.; Muelly, M.; Goodfellow, I.; Hardt, M.; and Kim, B. 2018. Sanity checks for saliency maps. *Advances in neural information processing systems*, 31.
- Arun, N.; Gaw, N.; Singh, P.; Chang, K.; Aggarwal, M.; Chen, B.; Hoebel, K.; Gupta, S.; Patel, J.; Gidwani, M.; et al. 2021. Assessing the trustworthiness of saliency maps for localizing abnormalities in medical imaging. *Radiology: Artificial Intelligence*, 3(6): e200267.
- Arunnehr, J.; et al. 2023. Deep learning-based real-world object detection and improved anomaly detection for surveillance videos. *Materials Today: Proceedings*, 80: 2911–2916.
- Augustin, M.; Boreiko, V.; Croce, F.; and Hein, M. 2022. Diffusion visual counterfactual explanations. *Advances in Neural Information Processing Systems*, 35: 364–377.
- Chen, Y.; Li, J.; Shan, S.; Wang, M.; and Hong, R. 2024. From static to dynamic: Adapting landmark-aware image models for facial expression recognition in videos. *IEEE Transactions on Affective Computing*.
- Chicco, D.; Warrens, M. J.; and Jurman, G. 2021. The coefficient of determination R-squared is more informative than SMAPE, MAE, MAPE, MSE and RMSE in regression analysis evaluation. *Peerj computer science*, 7: e623.
- Farhad, M.; Masud, M. M.; Beg, A.; Ahmad, A.; and Ahmed, L. 2023. A review of medical diagnostic video analysis using deep learning techniques. *Applied Sciences*, 13(11): 6582.
- Farid, K.; Schrodi, S.; Argus, M.; and Brox, T. 2023. Latent diffusion counterfactual explanations. *arXiv preprint arXiv:2310.06668*.
- Goyal, R.; Ebrahimi Kahou, S.; Michalski, V.; Materzynska, J.; Westphal, S.; Kim, H.; Haenel, V.; Freund, I.; Yianilos, P.; Mueller-Freitag, M.; et al. 2017. The” something something” video database for learning and evaluating visual common sense. In *Proceedings of the IEEE international conference on computer vision*, 5842–5850.
- Heusel, M.; Ramsauer, H.; Unterthiner, T.; Nessler, B.; and Hochreiter, S. 2017. Gans trained by a two time-scale update rule converge to a local nash equilibrium. *Advances in neural information processing systems*, 30.
- Hiley, L.; Preece, A.; Hicks, Y.; Chakraborty, S.; Gurrarn, P.; and Tomsett, R. 2020. Explaining motion relevance for activity recognition in video deep learning models. *arXiv preprint arXiv:2003.14285*.
- Jeanneret, G.; Simon, L.; and Jurie, F. 2022. Diffusion models for counterfactual explanations. In *Proceedings of the Asian conference on computer vision*, 858–876.
- Ji, Y.; Wang, Y.; and Kato, J. 2023. Spatial-temporal concept based explanation of 3d convnets. In *Proceedings of the IEEE/CVF Conference on Computer Vision and Pattern Recognition*, 15444–15453.
- Kanehira, A.; Takemoto, K.; Inayoshi, S.; and Harada, T. 2019. Multimodal explanations by predicting counterfactuality in videos. In *Proceedings of the IEEE/CVF Conference on Computer Vision and Pattern Recognition*, 8594–8602.
- Kolarik, M.; Sarnovsky, M.; Paralic, J.; and Babic, F. 2023. Explainability of deep learning models in medical video analysis: a survey. *PeerJ Computer Science*, 9: e1253.
- Li, Z.; Wang, W.; Li, Z.; Huang, Y.; and Sato, Y. 2021. Towards visually explaining video understanding networks with perturbation. In *Proceedings of the IEEE/CVF Winter Conference on Applications of Computer Vision*, 1120–1129.
- Nagelkerke, N. J.; et al. 1991. A note on a general definition of the coefficient of determination. *biometrika*, 78(3): 691–692.
- Ouyang, D.; He, B.; Ghorbani, A.; Yuan, N.; Ebinger, J.; Langlotz, C. P.; Heidenreich, P. A.; Harrington, R. A.; Liang, D. H.; Ashley, E. A.; et al. 2020. Video-based AI for beat-to-beat assessment of cardiac function. *Nature*, 580(7802): 252–256.
- Reynaud, H.; Qiao, M.; Dombrowski, M.; Day, T.; Razavi, R.; Gomez, A.; Leeson, P.; and Kainz, B. 2023. Feature-conditioned cascaded video diffusion models for precise echocardiogram synthesis. In *International Conference on Medical Image Computing and Computer-Assisted Intervention*, 142–152. Springer.
- Reynaud, H.; Vlontzos, A.; Dombrowski, M.; Gilligan Lee, C.; Beqiri, A.; Leeson, P.; and Kainz, B. 2022. D’artagnan: Counterfactual video generation. In *International Conference on Medical Image Computing and Computer-Assisted Intervention*, 599–609. Springer.
- Saha, A.; Gupta, S.; Ankireddy, S. K.; Chahine, K.; and Ghosh, J. 2024. Exploring explainability in video action recognition. In *Proceedings of the IEEE/CVF Conference on Computer Vision and Pattern Recognition*, 8176–8181.
- Simonyan, K.; and Zisserman, A. 2014. Very deep convolutional networks for large-scale image recognition. *arXiv preprint arXiv:1409.1556*.
- Smilkov, D.; Thorat, N.; Kim, B.; Viégas, F.; and Wattenberg, M. 2017. Smoothgrad: removing noise by adding noise. *arXiv preprint arXiv:1706.03825*.
- Song, J.; Meng, C.; and Ermon, S. 2020. Denoising diffusion implicit models. *arXiv preprint arXiv:2010.02502*.
- Stergiou, A.; Kapidis, G.; Kalliatakis, G.; Chrysoulas, C.; Veltkamp, R.; and Poppe, R. 2019. Saliency tubes: Visual explanations for spatio-temporal convolutions. In *2019 IEEE international conference on image processing (ICIP)*, 1830–1834. IEEE.
- Tang, Y.; Bi, J.; Xu, S.; Song, L.; Liang, S.; Wang, T.; Zhang, D.; An, J.; Lin, J.; Zhu, R.; et al. 2025. Video understanding with large language models: A survey. *IEEE Transactions on Circuits and Systems for Video Technology*.
- Tong, Z.; Song, Y.; Wang, J.; and Wang, L. 2022. Videomae: Masked autoencoders are data-efficient learners for self-supervised video pre-training. *Advances in neural information processing systems*, 35: 10078–10093.

Ullah, F. U. M.; Obaidat, M. S.; Ullah, A.; Muhammad, K.; Hijji, M.; and Baik, S. W. 2023. A comprehensive review on vision-based violence detection in surveillance videos. *ACM Computing Surveys*, 55(10): 1–44.

Unterthiner, T.; Van Steenkiste, S.; Kurach, K.; Marinier, R.; Michalski, M.; and Gelly, S. 2018. Towards accurate generative models of video: A new metric & challenges. *arXiv preprint arXiv:1812.01717*.

Varshney, P.; Lucieri, A.; Balada, C.; Dengel, A.; and Ahmed, S. 2024. Generating counterfactual trajectories with latent diffusion models for concept discovery. In *International Conference on Pattern Recognition*, 138–153. Springer.

Wachter, S.; Mittelstadt, B.; and Russell, C. 2017. Counterfactual explanations without opening the black box: Automated decisions and the GDPR. *Harv. JL & Tech.*, 31: 841.

Wang, Y.; Sun, Y.; Huang, Y.; Liu, Z.; Gao, S.; Zhang, W.; Ge, W.; and Zhang, W. 2022. Ferv39k: A large-scale multi-scene dataset for facial expression recognition in videos. In *Proceedings of the IEEE/CVF conference on computer vision and pattern recognition*, 20922–20931.

Wang, Z.; Bovik, A. C.; Sheikh, H. R.; and Simoncelli, E. P. 2004. Image quality assessment: from error visibility to structural similarity. *IEEE transactions on image processing*, 13(4): 600–612.

Yang, Z.; Teng, J.; Zheng, W.; Ding, M.; Huang, S.; Xu, J.; Yang, Y.; Hong, W.; Zhang, X.; Feng, G.; et al. 2024. Cogvideox: Text-to-video diffusion models with an expert transformer. *arXiv preprint arXiv:2408.06072*.

Yurtsever, E.; Lambert, J.; Carballo, A.; and Takeda, K. 2020. A survey of autonomous driving: Common practices and emerging technologies. *IEEE access*, 8: 58443–58469.

Zhang, R.; Isola, P.; Efros, A. A.; Shechtman, E.; and Wang, O. 2018. The unreasonable effectiveness of deep features as a perceptual metric. In *Proceedings of the IEEE conference on computer vision and pattern recognition*, 586–595.

Zong, L.; Lin, W.; Zhou, J.; Liu, X.; Zhang, X.; Xu, B.; and Wu, S. 2025. Text-Guided Fine-grained Counterfactual Inference for Short Video Fake News Detection. In *Proceedings of the AAAI Conference on Artificial Intelligence*, volume 39, 1237–1245.

## Supplementary Material

### Evaluation Metrics

This section formally defines the metrics used to evaluate the generated counterfactual video explanations. A diverse set of metrics was used to assess the predictive performance and the perceptual quality of the counterfactuals. Predictive performance was evaluated using regression and classification accuracy metrics. For regression tasks, the coefficient of determination ( $R^2$ ), root mean square error (RMSE), and mean absolute error (MAE) were adopted to quantify the validity of the counterfactuals. The Flip Ratio (FR) was used in classification tasks to quantify the success rate of the generated counterfactuals. In addition to predictive performance, the quality of the generated counterfactuals was assessed using perceptual and distributional similarity metrics. The structural similarity index measure (SSIM) and the learned perceptual image patch similarity (LPIPS) were used to capture visual similarity between factual and counterfactual instances. The Fréchet inception distance (FID) measures the distributional alignment of generated images with the real data distribution, while the Fréchet video distance (FVD) extends this evaluation to the temporal domain of videos. Together, these metrics provide a comprehensive assessment of the effectiveness, realism, and temporal coherence of the generated counterfactuals.

**$R^2$  (Coefficient of Determination)** The coefficient of determination  $R^2$  (Nagelkerke et al. 1991) was computed as:

$$R^2 = 1 - \frac{\sum_{i=1}^N (y'_i - \hat{y}_i)^2}{\sum_{i=1}^N (y'_i - \bar{y})^2},$$

where  $y'_i$  and  $\hat{y}_i$  denote the target and predicted values,  $\bar{y}$  is the mean of the target values, and  $N$  is the number of samples.  $R^2$  was chosen to quantify how well the regression model explains the variance in the target variable, which is important for determining whether counterfactual generation degrades predictive performance.

**Root Mean Square Error (RMSE)** The RMSE was calculated as:

$$\text{RMSE} = \sqrt{\frac{1}{N} \sum_{i=1}^N (y'_i - \hat{y}_i)^2}.$$

RMSE was selected to detect substantial deviations between the predicted and target continuous outputs for counterfactual videos. Large RMSE values may indicate that the generated counterfactuals deviate excessively from the target distribution.

**Mean Absolute Error (MAE)** The MAE was computed as:

$$\text{MAE} = \frac{1}{N} \sum_{i=1}^N |y'_i - \hat{y}_i|.$$

MAE was included to provide an interpretable measure of the average deviation between the predicted and target values. Together with RMSE, it ensures that both typical and

extreme prediction errors are monitored during counterfactual evaluation (Chicco, Warrens, and Jurman 2021).

**Flip Ratio (FR)** For classification tasks, the Flip Ratio was used to measure the validity of counterfactuals. It is the proportion of counterfactual instances that successfully alter the model’s prediction to the target class  $y'$ :

$$\text{FR} = \frac{\sum_{i=1}^N \mathbf{I}[f_\phi(x'_i) = y']}{N},$$

where  $f_\phi(\cdot)$  denotes the classifier,  $x'_i$  the generated counterfactual, and  $\mathbf{I}[\cdot]$  the indicator function. FR assesses counterfactual explanations’ primary goal, changing the model’s decision while ensuring the modified instance remains realistic.

**Structural Similarity Index Measure (SSIM)** The SSIM (Wang et al. 2004) was computed as:

$$\text{SSIM}(x, x') = \frac{(2\mu_x\mu_{x'} + C_1)(2\sigma_{xx'} + C_2)}{(\mu_x^2 + \mu_{x'}^2 + C_1)(\sigma_x^2 + \sigma_{x'}^2 + C_2)},$$

where  $\mu_x$  and  $\mu_{x'}$  are mean intensities of the factual and counterfactual videos,  $\sigma_x^2$  and  $\sigma_{x'}^2$  are variances,  $\sigma_{xx'}$  is the covariance, and  $C_1, C_2$  are small constants. SSIM was chosen to evaluate the preservation of structural and luminance information, ensuring that counterfactuals maintain the spatial coherence of the original input.

**Learned Perceptual Image Patch Similarity (LPIPS)** The LPIPS (Zhang et al. 2018) metric was calculated as:

$$\text{LPIPS}(x, x') = \sum_l \frac{1}{H_l W_l} \sum_{h,w} \|\hat{x}'_{hw}{}^l - \hat{x}_{hw}{}^l\|_2^2,$$

where  $\hat{x}^l$  and  $\hat{x}'^l$  are normalized deep features from layer  $l$  of a pretrained VGG network (Simonyan and Zisserman 2014), and  $H_l$  and  $W_l$  denote the spatial dimensions at that layer. LPIPS was computed per frame and then averaged across all frames for videos. LPIPS was adopted to capture perceptual differences between factual and counterfactual instances in a way that aligns with human visual similarity judgments, beyond simple pixel-wise comparisons.

**Fréchet Inception Distance (FID)** The FID (Heusel et al. 2017) was computed as:

$$\text{FID}(x, x') = \|\mu_x - \mu_{x'}\|_2^2 + \text{Tr} \left( \Sigma_x + \Sigma_{x'} - 2(\Sigma_x \Sigma_{x'})^{1/2} \right),$$

where  $(\mu_x, \Sigma_x)$  and  $(\mu_{x'}, \Sigma_{x'})$  denote the means and covariances of deep features extracted from the factual and counterfactual samples, respectively. FID<sup>2</sup> was selected to quantify the distributional similarity between factual and counterfactual data in a deep feature space, ensuring that counterfactuals remain close to the manifold of realistic samples.

<sup>2</sup>The implementation of FID and FVD metrics was taken from <https://github.com/universome/stylegan-v?tab=readme-ov-file>.

Method	T	$\lambda_c$	$R^2 \uparrow$	MAE $\downarrow$	RMSE $\downarrow$	SSIM $\uparrow$	LPIPS $\downarrow$
LD-ViCE-SG	5	0.05	0.52	5.07	8.14	<b>0.78</b>	<b>0.14</b>
LD-ViCE-SG	5	0.10	0.78	3.17	5.45	<b>0.78</b>	0.15
LD-ViCE-SG	5	0.15	0.86	2.44	4.35	<b>0.78</b>	0.15
LD-ViCE-SG	10	0.05	0.88	2.23	4.12	0.77	0.15
LD-ViCE-SG	10	0.10	0.96	1.17	2.42	0.76	0.16
LD-ViCE-SG	10	0.15	0.98	0.80	1.70	0.76	0.16
LD-ViCE-SG	15	0.05	0.95	1.37	2.62	0.76	0.16
LD-ViCE-SG	15	0.10	0.98	0.70	1.43	0.75	0.16
LD-ViCE-SG	15	0.15	<b>0.99</b>	<b>0.50</b>	<b>1.02</b>	0.75	0.17

Table 3: Comparison of LD-ViCE performance on the EchoNet-Dynamic regression task for varying denoising inference steps ( $T$ ) and gradient loss scales ( $\lambda_c$ ). Results are reported on 1,288 videos from the validation set. Higher values of both parameters consistently improved regression accuracy while maintaining comparable perceptual quality. Best values are highlighted in bold. Based on these results,  $\lambda_c = 0.15$  and  $T = 15$  were selected as optimal values for subsequent experiments.

Method	$t_{\text{sup}}$	$R^2 \uparrow$	MAE $\downarrow$	RMSE $\downarrow$	SSIM $\uparrow$	LPIPS $\downarrow$
LD-ViCE-SGA	0.01	<b>0.98</b>	<b>1.12</b>	<b>1.75</b>	0.79	0.16
LD-ViCE-SGA	0.03	0.90	2.78	3.75	0.84	0.13
LD-ViCE-SGA	0.05	0.76	4.41	5.72	0.87	0.10
LD-ViCE-SGA	0.07	0.59	5.97	7.55	<b>0.90</b>	<b>0.08</b>

Table 4: Comparison of LD-ViCE performance on the EchoNet-Dynamic regression task for different artifact suppression thresholds used to reduce denoising artifacts. Results are reported on 1288 videos from the validation set. Best values are highlighted in bold. An intermediate threshold ( $t_{\text{sup}} = 0.03$ ) achieved the best balance between regression accuracy and perceptual quality.

**Fréchet Video Distance (FVD)** The FVD (Unterthiner et al. 2018) was computed analogously to FID, but the features were extracted from an Inflated 3D ConvNet (I3D) pretrained on Kinetics-400. FVD was included to extend distributional similarity assessment to the temporal domain, ensuring that generated video counterfactuals are visually plausible and temporally coherent.

### Ablation Studies

In LD-ViCE, counterfactual generation is influenced by three key hyperparameters: the gradient loss scale ( $\lambda_c$ ), the number of denoising inference steps ( $T$ ), and the artifact suppression threshold ( $t_{\text{sup}}$ ). Systematic ablation studies were conducted to assess their impact on the quality of generated counterfactuals. Initially,  $\lambda_c$  and  $T$  were varied using the SmoothGrad (SG) variant, as they directly control the strength of the classifier guidance and quality of generated sequences. The number of noise perturbations  $N$  for SmoothGrad was set to 10, balancing inference efficiency with effective suppression of noisy gradients. After identifying optimal values of  $\lambda_c$  and  $T$ , the artifact suppression threshold ( $t_{\text{sup}}$ ) was tuned using the SGA variant to improve visual quality further and reduce denoising artifacts. Subsequently, the raw gradient (RG) variant was then evaluated using the same  $\lambda_c$  and  $T$  settings to ensure consistency across variants. Ablation experiments were performed independently on the EchoNet-Dynamic and FERV39K datasets to account for domain-specific differences in video charac-

teristics and complexity.

### Hyperparameters for the EchoNet-Dynamic Dataset

The performance of LD-ViCE was evaluated using regression accuracy metrics ( $R^2$ , MAE, and RMSE) to measure the effectiveness of prediction shifts, and perceptual similarity metrics (SSIM and LPIPS) to assess structural preservation and visual fidelity of the generated counterfactuals.

**Gradient Loss Scale and Denoising Steps** In counterfactual generation, increasing the number of denoising inference steps ( $T$ ) provides the model with more opportunities to iteratively refine the generated video and incorporate classifier guidance. The number of denoising steps corresponds to the same number of steps for which noise is added initially. While higher  $T$  values can improve reconstruction fidelity and enhance prediction shifts, excessive values may also lead to over-modification of the input, potentially affecting perceptual quality. Similarly, increasing the gradient loss scale ( $\lambda_c$ ) strengthens the influence of classifier gradients during generation.  $\lambda_c$  can enhance counterfactual success rates by steering the generation towards the desired prediction change more effectively. However, overly high values may introduce out-of-distribution noise, which can manifest as unrealistic structures or subtle artifacts in the generated frames.

Table 3 shows that regression accuracy consistently im-

Method	T	$\lambda_c$	FR $\uparrow$	SSIM $\uparrow$	LPIPS $\downarrow$	FID $\downarrow$	FVD $\downarrow$
LD-ViCE-SG	5	55	0.984	<b>0.846</b>	<b>0.165</b>	<b>4.081</b>	<b>29.24</b>
LD-ViCE-SG	5	60	0.986	0.845	0.166	4.124	29.99
LD-ViCE-SG	5	65	0.988	0.844	0.167	4.193	30.57
LD-ViCE-SG	10	55	0.998	0.832	0.180	4.421	30.56
LD-ViCE-SG	10	60	0.999	0.831	0.182	4.451	30.65
LD-ViCE-SG	10	65	0.999	0.830	0.183	4.572	31.73
LD-ViCE-SG	15	55	<b>1.000</b>	0.823	0.191	4.692	31.51
LD-ViCE-SG	15	60	<b>1.000</b>	0.821	0.192	4.790	32.05
LD-ViCE-SG	15	65	<b>1.000</b>	0.820	0.194	4.889	32.58

Table 5: Quantitative evaluation of LD-ViCE on the FERV39K classification task for varying denoising inference steps ( $T$ ) and gradient loss scales ( $\lambda_c$ ). Results are reported on 7,847 samples from the test set. Higher values of both parameters generally improve classification success, with a slight trade-off in perceptual quality. Best values are highlighted in bold.  $\lambda_c = 55$  and  $T = 5$  were selected as optimal values for subsequent experiments.

Method	$t_{\text{sup}}$	FR $\uparrow$	SSIM $\uparrow$	LPIPS $\downarrow$	FID $\downarrow$	FVD $\downarrow$
LD-ViCE-SGA	0.03	<b>0.977</b>	0.862	0.213	12.278	81.01
LD-ViCE-SGA	0.05	0.955	0.888	0.191	12.997	71.73
LD-ViCE-SGA	0.07	0.914	0.910	0.163	11.520	55.62
LD-ViCE-SGA	0.1	0.814	<b>0.934</b>	<b>0.127</b>	<b>9.089</b>	<b>35.72</b>

Table 6: Quantitative evaluation of LD-ViCE on the FERV39K classification task for varying artifact suppression thresholds ( $t_{\text{sup}}$ ) applied to reduce denoising artifacts. Results are reported on 7,847 samples from the test set. Best values are highlighted in bold. A threshold ( $t_{\text{sup}} = 0.10$ ) provided the best trade-off, effectively reducing artifacts while maintaining classification success and perceptual quality.

proved with higher values of  $T$  and  $\lambda_c$ . Perceptual metrics (SSIM and LPIPS) exhibited minor variations, indicating that the accuracy gains were achieved with only slight visual quality degradation. Based on these results,  $\lambda_c = 0.15$  and  $T = 15$  were selected for subsequent experiments on the EchoNet-Dynamic dataset.

**Artifact Suppression Threshold** The artifact suppression threshold ( $t_{\text{sup}}$ ) mitigates denoising-related artifacts that may appear during counterfactual generation. Such artifacts typically result from denoising process and may include high-frequency distortions, unnatural textures, or subtle structural inconsistencies in the generated frames. By applying this threshold, minor updates below  $t_{\text{sup}}$  are suppressed, thereby reducing the visual impact of residual denoising errors while preserving the overall structural coherence of the video.

The effect of varying  $t_{\text{sup}}$  was evaluated using the previously selected optimal values of  $\lambda_c$  and  $T$  as shown in Table 4. Lower thresholds retained more fine-grained details and preserved residual denoising artifacts, reducing perceptual quality. Conversely, higher thresholds significantly reduced artifacts but at the cost of oversmoothing and reduced regression accuracy. An intermediate threshold value 0.03 offered the best trade-off, providing perceptually cleaner counterfactuals while maintaining competitive regression accuracy. This value was therefore adopted for all subsequent experiments on the EchoNet-Dynamic dataset.

## Hyperparameters for the FERV39K Dataset

The performance of LD-ViCE on the FERV39K dataset was evaluated using the classification success rate (Flip Ratio, FR), perceptual similarity measures (SSIM and LPIPS), and distributional alignment metrics (FID and FVD). The FR measures counterfactual effectiveness in altering predictions, SSIM and LPIPS evaluate visual similarity to factual videos, and FID and FVD assess realism and temporal coherence of generated counterfactual sequences. For each sample, the target class was randomly selected from the set of non-predicted classes. To ensure reproducibility, the selection was kept consistent across runs by fixing the random seed.

**Gradient Loss Scale and Denoising Steps** A similar impact of the denoising inference steps ( $T$ ) and gradient loss scale ( $\lambda_c$ ) was observed on the FERV39K dataset as in the EchoNet-Dynamic experiments. Higher values of these hyperparameters improved classification performance but slightly reduced perceptual quality. As shown in Table 5, FR improved consistently with higher values of the denoising inference steps ( $T$ ) and the gradient loss scale ( $\lambda_c$ ). In particular, increasing  $T$  enhanced classifier guidance incorporation, while larger  $\lambda_c$  values strengthened the influence of classifier gradients, leading to more decisive counterfactual modifications. However, perceptual metrics (SSIM and LPIPS) declined slightly at higher parameter settings, and distributional metrics (FID and FVD) increased mod-

erately, indicating a small trade-off between classification accuracy and perceptual realism. A balance between classification performance and perceptual quality was achieved with  $\lambda_c = 55$  and  $T = 5$ , which were selected as the optimal settings for subsequent experiments on the FERV39K dataset.

**Artifact Suppression Threshold** A similar role of the artifact suppression threshold ( $t_{\text{sup}}$ ) was observed for the FERV39K dataset as in the EchoNet-Dynamic experiments. Higher thresholds reduced denoising artifacts and improved perceptual and distributional alignment metrics (SSIM, LPIPS, FID, FVD) but lowered classification success (FR), while lower thresholds preserved accuracy at the cost of leaving residual artifacts. Table 6 indicates that increasing  $t_{\text{sup}}$  progressively improved visual and distributional quality but led to decreased FR. A threshold of  $t_{\text{sup}} = 0.10$  offered the best perceptual quality and distributional alignment, making it the preferred choice for subsequent experiments on the FERV39K dataset.

### EchoNet-Dynamic Dataset Counterfactual Results

Counterfactual videos were generated using the three LD-ViCE variants (RG, SG, and SGA) under the selected optimal hyperparameters. Figure 5 and 6 show frames produced by the RG variant exhibited noticeable noisy artifacts, whereas such artifacts were not observed in the SG and SGA variants. This demonstrates the effectiveness of SmoothGrad-based approaches in eliminating noisy gradient effects and producing visually clean and coherent counterfactual frames. The difference maps highlight the regions that change between the factual and counterfactual images.

Figure 7 and 8 provide a qualitative comparison on the EchoNet-Dynamic dataset, highlighting LD-ViCE’s ability to generate counterfactual explanations that are better aligned with the target regression values compared to baseline methods. The results illustrate both the effectiveness of classifier-guided generation and the visual fidelity of the produced counterfactuals.

### FERV39K Dataset Counterfactual Results

Figures 9 and 10 illustrate qualitative counterfactual examples generated by the three variants of LD-ViCE (RG, SG, and SGA) together with their corresponding difference maps. The counterfactual transformation shifts the predicted emotion from *sad* to *happy* in as shown in Figure 9. The generated samples exhibit class-specific facial modifications, such as a subtle upward lift of the cheeks and a softening of the mouth curvature, consistent with features typically associated with happiness. Figure 10 illustrates another transformation set that changes the predicted emotion from *angry* to *sad*. Here, the modifications reduce the intensity of the brow furrow, relax the upper eyelid tension, and lower the mouth corners to convey sadness. The RG variant produces widespread pixel-level changes across the face in both examples, as seen in the difference maps. The SG variant substantially reduces spatial noise, concentrating modifications more effectively within relevant facial

regions, although some non-critical variations persist. The SGA variant shows the most compact and targeted activations. Different maps reveal modifications concentrated in semantically meaningful regions such as the cheeks, eyes, and mouth, while preserving the remainder of the face unchanged. This behavior confirms the effectiveness of the artifact suppression mechanism in focusing counterfactual changes on class-discriminative features.

In addition to these examples, counterfactual results were generated for two representative samples from each of the seven emotion classes, with each sample transformed into all other non-predicted target classes, as shown in Figures 11–24. The subsequent figures demonstrate LD-ViCE’s ability to produce semantically meaningful modifications across a diverse range of source–target emotion transitions.

## Something- Something V2 Dataset Counterfactual Results

The Something-Something V2 (SSv2) dataset is a highly complex benchmark for counterfactual generation. Its large number of action classes spans a wide range of object types, interactions, and motion patterns, requiring substantial and perceptually consistent changes across multiple frames to transform one class into another. Generating such counterfactuals is challenging, as the modifications must convincingly alter spatial appearance and temporal dynamics to reflect the target class. For this study, only qualitative evaluation was performed by selecting representative source–target class pairs to examine the ability of LD-ViCE to produce semantically meaningful counterfactuals. Figures 25 and 26 show transformations from source class *Bending something so that it deforms* to target class *Bending something until it breaks*. The generated counterfactuals change the correct interaction region. However, the modifications often fail to capture the perceptual cues of an actual break event, such as the appearance of a distinct post-break object deformation.

Similarly, Figures 27 and 28 illustrate transformations from source class *Pouring something into something* to target class *Pouring something into something until it overflows*. While changes are observed on the upper surface of the container, creating the effect of it being filled. However, no visual evidence of liquid spilling or overflowing is present, which limits the semantic faithfulness of the generated counterfactual.

Across all examples, the RG variant produces widespread, diffuse changes that extend beyond the relevant interaction region. The SG variant reduces this noise, leading to more localized modifications. The SGA variant achieves the most spatially compact and targeted alterations, focusing on changes in the expected action-critical areas. However, the generated counterfactuals, while frequently classified as the target class with high confidence, do not always convey semantically faithful visual evidence for the intended action change. This mismatch suggests that the model may rely on dataset biases or non-discriminative background/context cues to trigger the classifier, rather than learning robust, class-specific visual–temporal features. The high diversity of SSv2 classes, variation in object appearance, and com-

plex temporal dependencies contribute to this difficulty.

### **Multimedia Supplementary Material**

All videos corresponding to the qualitative results shown in the main paper and this supplementary document are provided in the accompanying multimedia supplementary material.

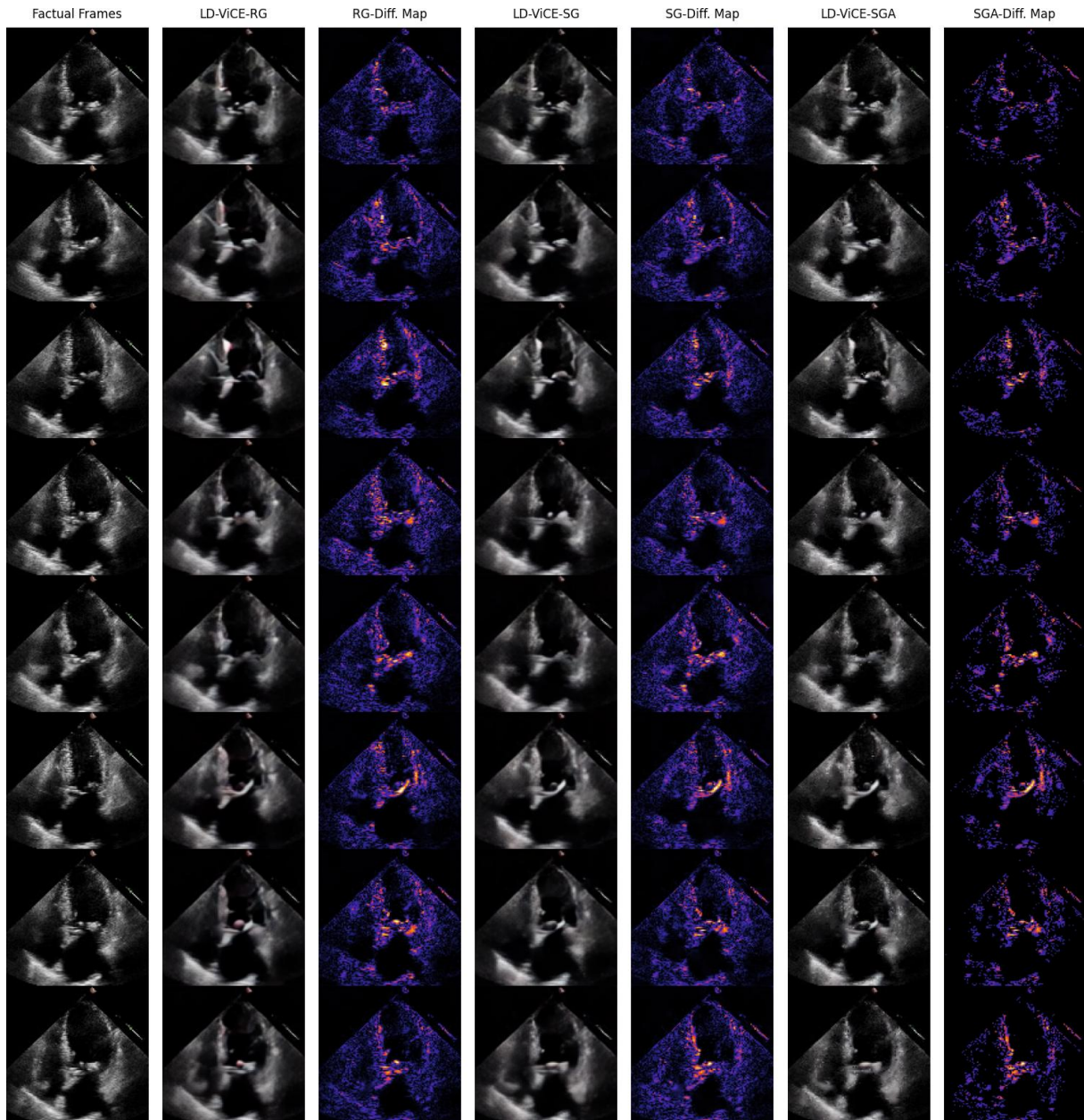


Figure 5: Qualitative counterfactual results generated by LD-ViCE variants (RG, SG, and SGA) on a sample of the EchoNet-Dynamic dataset, shown with corresponding difference maps between the factual and counterfactual frames. Eight frames are displayed for each video. SG and SGA variants eliminate noisy artifacts present in RG, producing visually cleaner and more coherent counterfactuals.

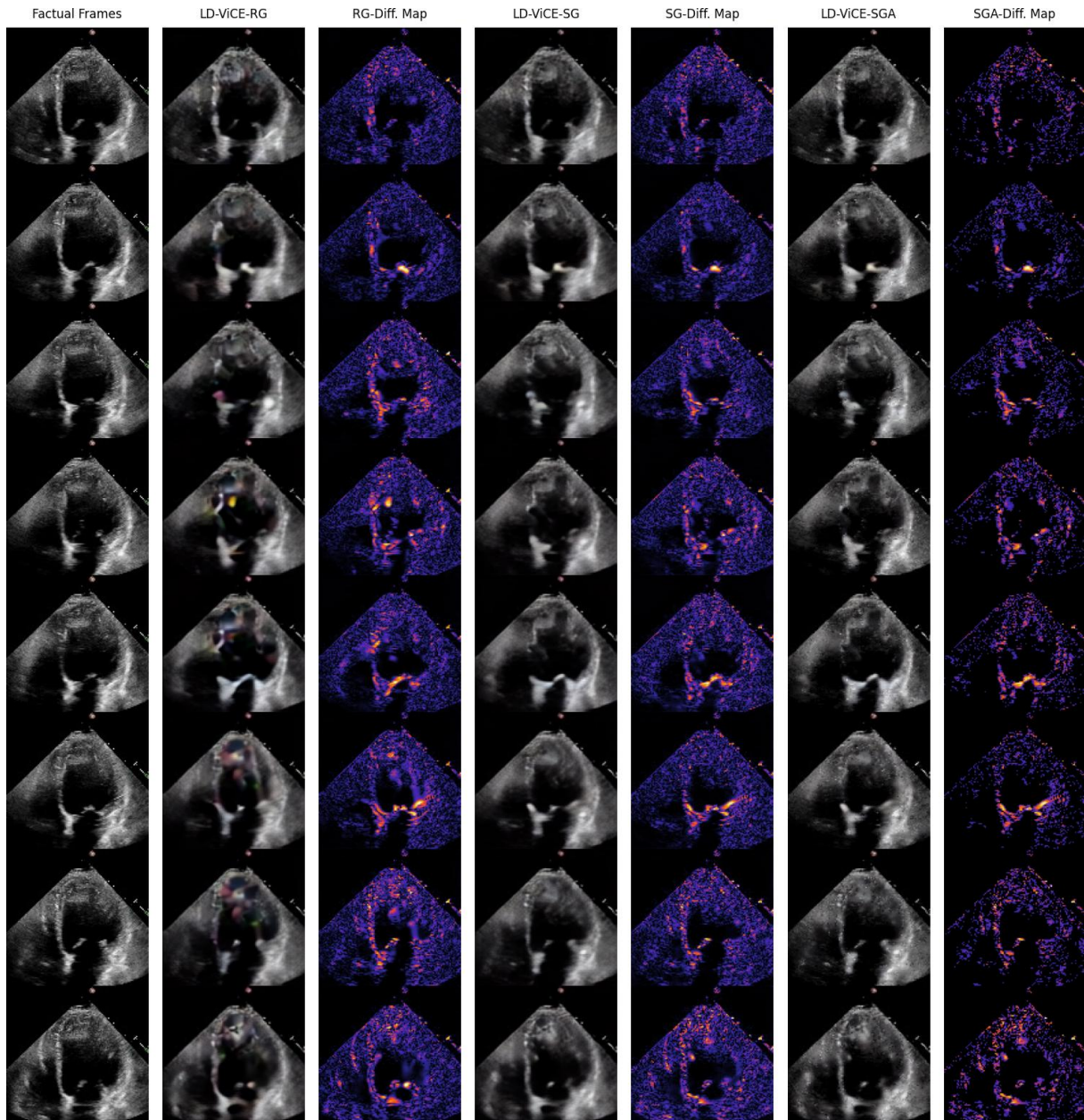
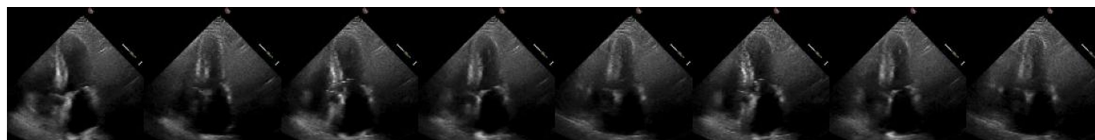
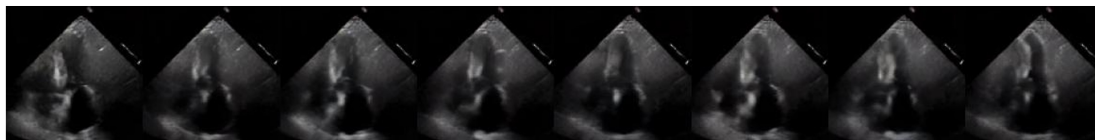


Figure 6: Qualitative counterfactual results generated by LD-ViCE variants (RG, SG, and SGA) on a sample of the EchoNet-Dynamic dataset, shown with corresponding difference maps between the factual and counterfactual frames. Eight frames are displayed for each video. SG and SGA variants eliminate noisy artifacts present in RG, producing visually cleaner and more coherent counterfactuals.

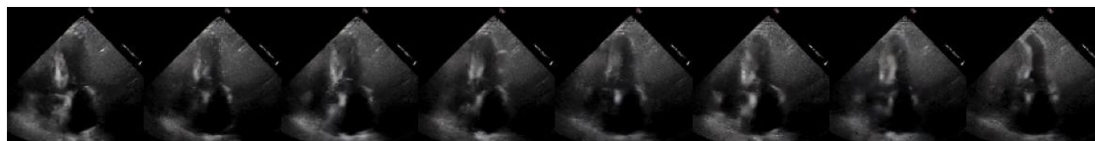
Original Video  
Pred LVEF : 64.2  
Target LVEF : 35.8



LD-ViCE-SG (Ours)  
Pred LVEF : 35.7



LD-ViCE-SGA (Ours)  
Pred LVEF : 34.4



Reynaud et al. (2023)  
Pred LVEF : 30.4

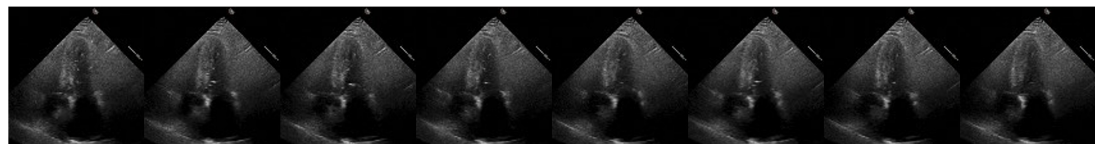
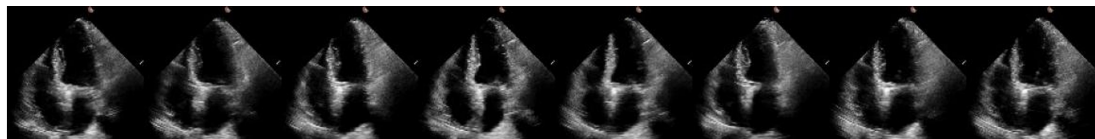
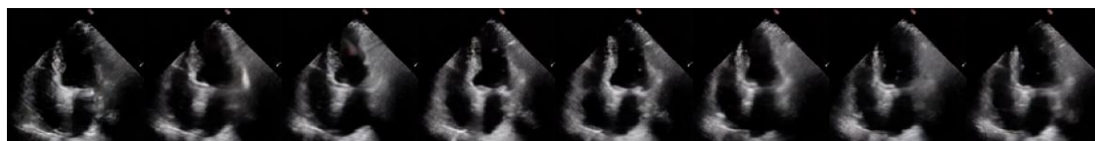


Figure 7: Qualitative comparison of counterfactual explanations on the EchoNet-Dynamics dataset, demonstrating LD-ViCE’s improved alignment between counterfactual explanations and target regression values. The first row displays eight frames from the original video, while the following rows show counterfactuals generated using LD-ViCE-SG, LD-ViCE-SGA, and EchoDiffusion (Reynaud et al. 2023), respectively. The predicted and target LVEF values are given on the left.

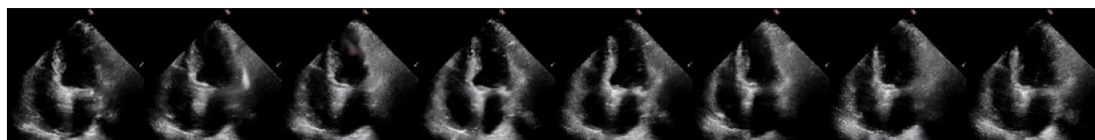
Original Video  
Pred LVEF : 44.7  
Target LVEF : 55.3



LD-ViCE-SG (Ours)  
Pred LVEF : 55.4



LD-ViCE-SGA (Ours)  
Pred LVEF : 56.7



Reynaud et al. (2023)  
Pred LVEF : 59.6

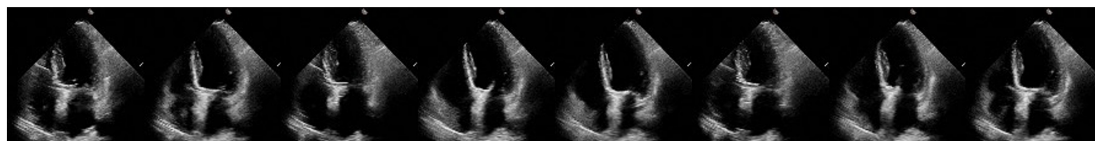


Figure 8: Qualitative comparison of counterfactual explanations on the EchoNet-Dynamics dataset, demonstrating LD-ViCE’s improved alignment between counterfactual explanations and target regression values. The first row displays eight frames from the original video, while the following rows show counterfactuals generated using LD-ViCE-SG, LD-ViCE-SGA, and EchoDiffusion (Reynaud et al. 2023), respectively. The predicted and target LVEF values are given on the left.

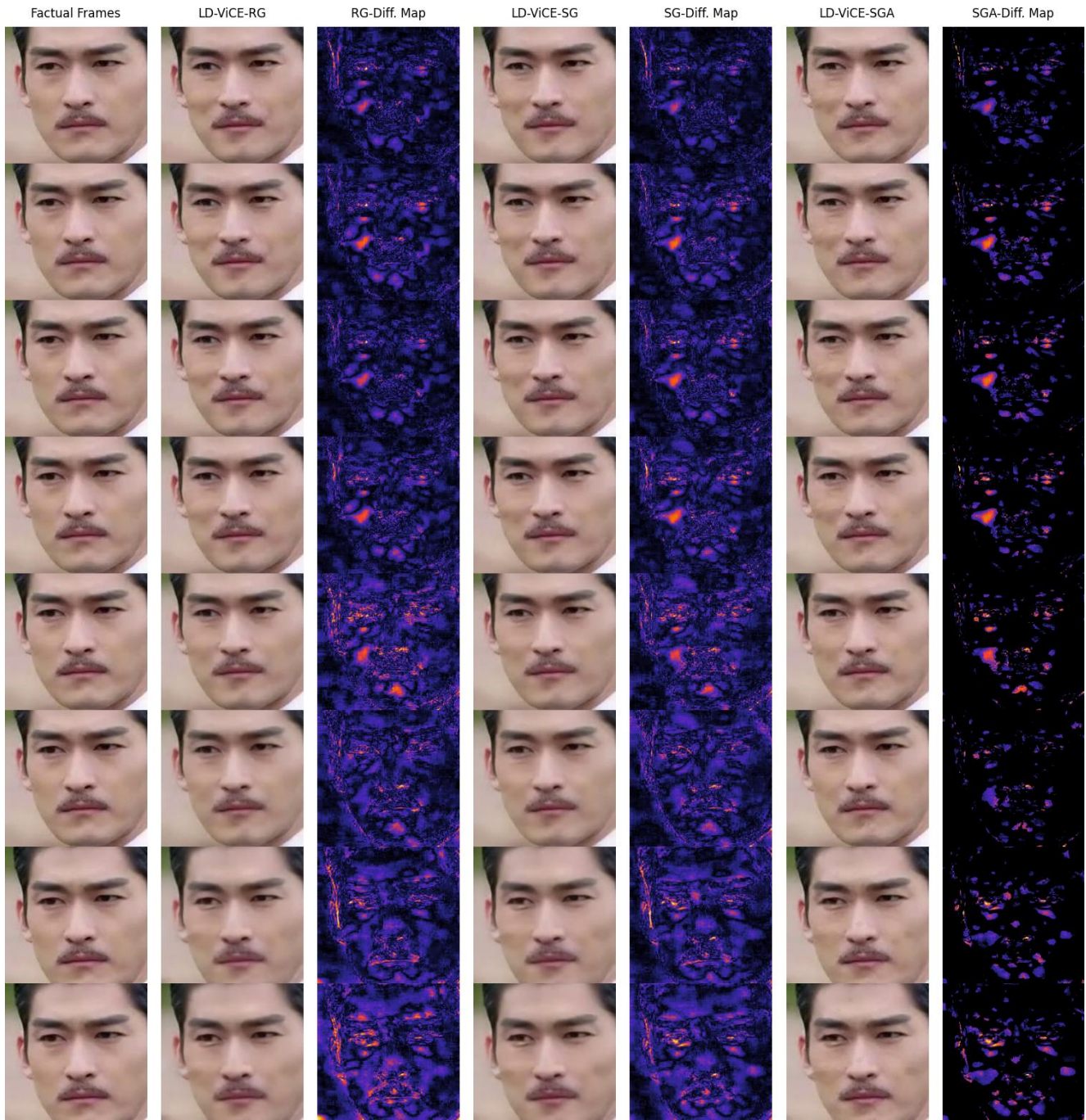


Figure 9: Qualitative counterfactual results for transforming the predicted emotion from *sad* to *happy* using the three variants of LD-ViCE (RG, SG, and SGA) on the FERV39K dataset, with corresponding difference maps. Class-specific modifications, such as cheek lifting and softening of the mouth curvature, are evident in the counterfactuals. The RG variant produces widespread changes, SG reduces irrelevant variations, and SGA focuses on modifications in semantically relevant facial regions.

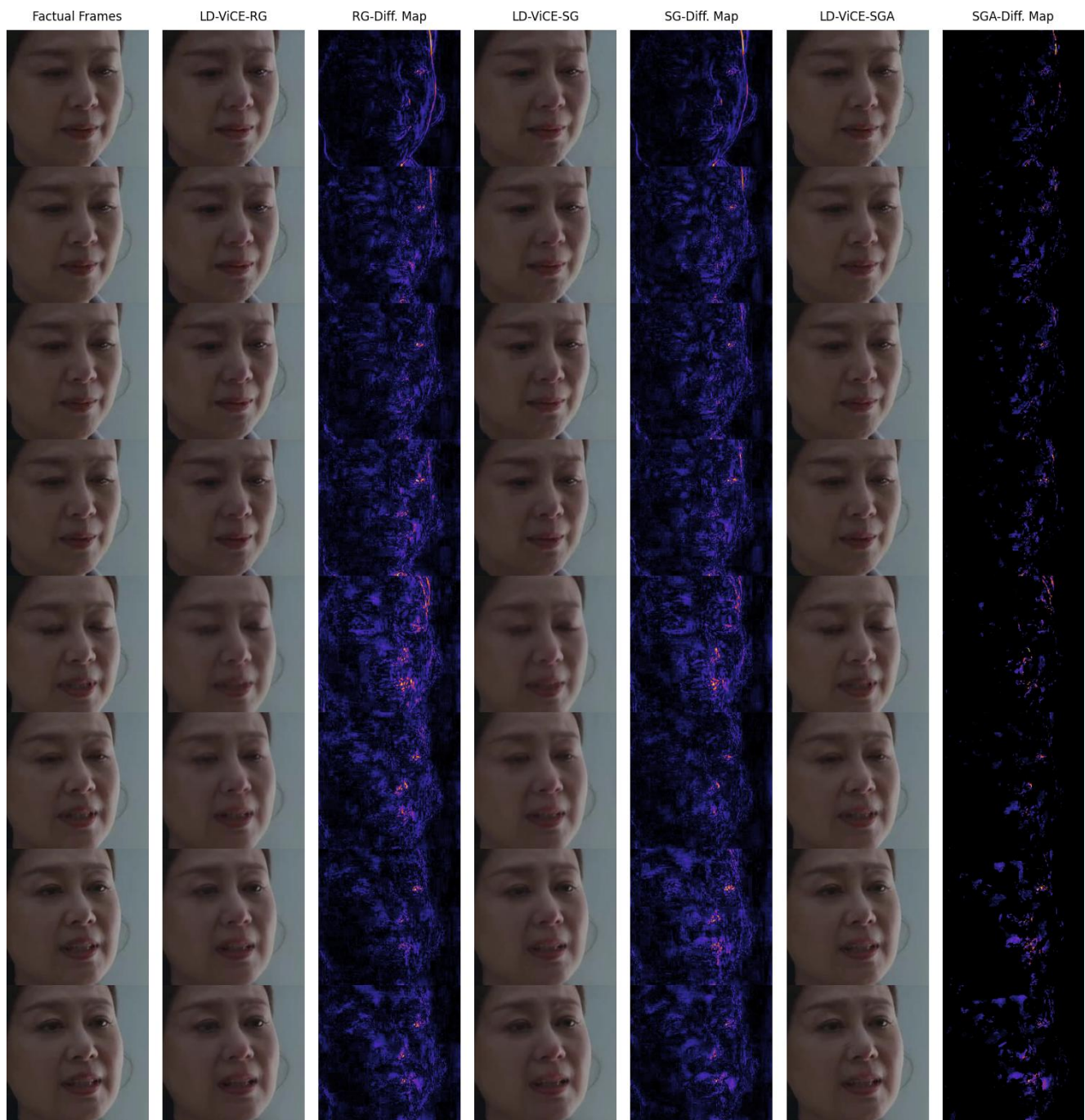


Figure 10: Qualitative counterfactual results for transforming the predicted emotion from *angry* to *sad* using the three variants of LD-ViCE (RG, SG, and SGA) on the FERV39K dataset, with corresponding difference maps. Class-specific modifications include reduced brow tension, lowered mouth corners, and relaxed eye regions. RG introduces widespread pixel-level changes, SG localizes them more effectively, and SGA concentrates modifications in the most discriminative facial regions.



Figure 11: Qualitative counterfactual results generated by LD-ViCE on the FERV39K dataset, transforming the predicted class emotion *Angry* into each of the other emotion classes. The generated counterfactuals display distinct, class-consistent facial dynamics that align with the target emotional categories.

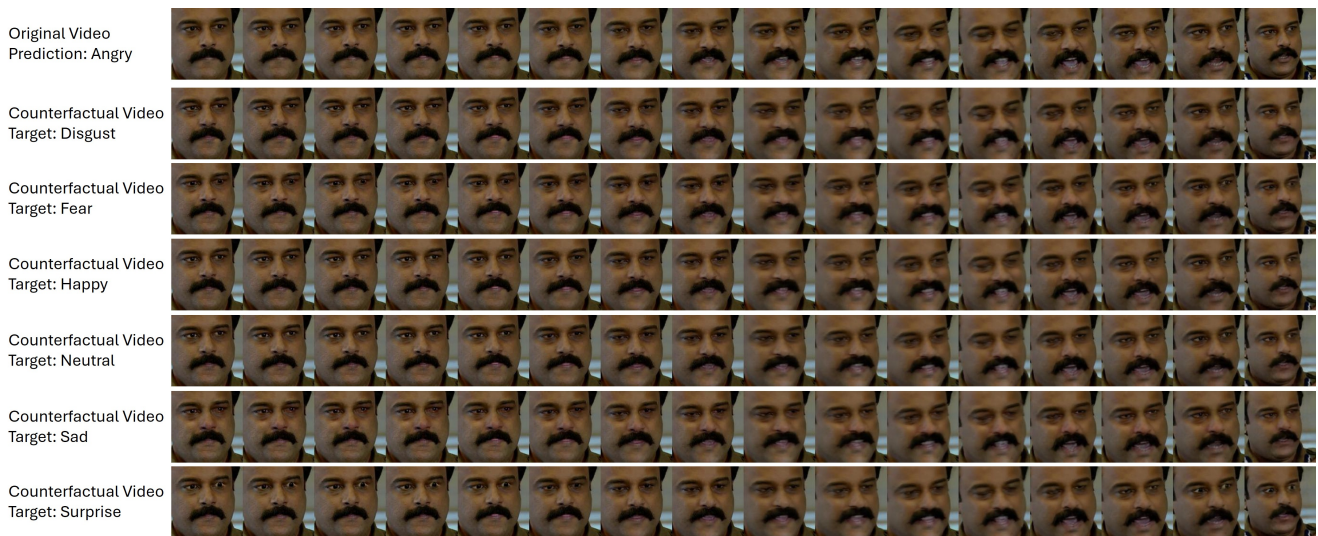


Figure 12: Qualitative counterfactual results generated by LD-ViCE on the FERV39k dataset, transforming the predicted class emotion *Angry* into each of the other emotion classes. The generated counterfactuals exhibit distinct and class-consistent facial dynamics corresponding to the desired emotional categories.



Figure 13: Qualitative counterfactual results generated by LD-ViCE on the FERV39k dataset, transforming the predicted class emotion *Disgust* into each of the other emotion classes. The generated counterfactuals exhibit distinct and class-consistent facial dynamics corresponding to the desired emotional categories.



Figure 14: Qualitative counterfactual results generated by LD-ViCE on the FERV39k dataset, transforming the predicted class emotion *Disgust* into each of the other emotion classes. The generated counterfactuals exhibit distinct and class-consistent facial dynamics corresponding to the desired emotional categories.



Figure 15: Qualitative counterfactual results generated by LD-ViCE on the FERV39k dataset, transforming the predicted class emotion *Fear* into each of the other emotion classes. The generated counterfactuals exhibit distinct and class-consistent facial dynamics corresponding to the desired emotional categories.



Figure 16: Qualitative counterfactual results generated by LD-ViCE on the FERV39k dataset, transforming the predicted class emotion *Fear* into each of the other emotion classes. The generated counterfactuals exhibit distinct and class-consistent facial dynamics corresponding to the desired emotional categories.



Figure 17: Qualitative counterfactual results generated by LD-ViCE on the FERV39k dataset, transforming the predicted class emotion *Happy* into each of the other emotion classes. The generated counterfactuals exhibit distinct and class-consistent facial dynamics corresponding to the desired emotional categories.

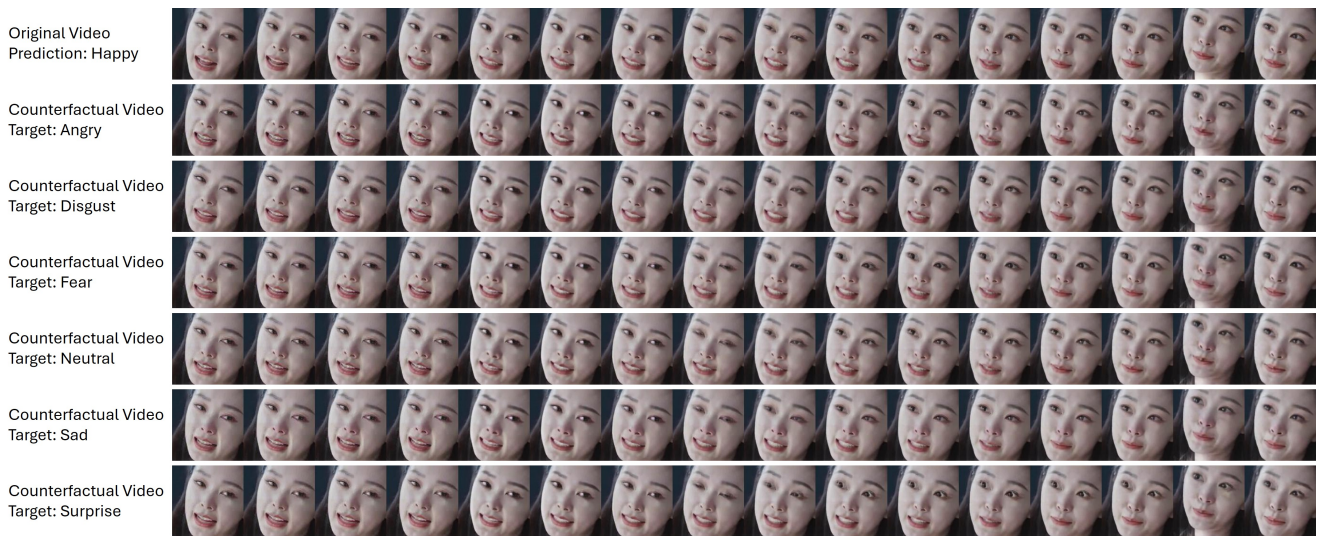


Figure 18: Qualitative counterfactual results generated by LD-ViCE on the FERV39k , transforming the predicted class emotion *Happy* into each of the other emotion classes. The generated counterfactuals exhibit distinct and class-consistent facial dynamics corresponding to the desired emotional categories.



Figure 19: Qualitative counterfactual results generated by LD-ViCE on the FERV39k dataset, transforming the predicted class emotion *Neutral* into each of the other emotion classes. The generated counterfactuals exhibit distinct and class-consistent facial dynamics corresponding to the desired emotional categories.



Figure 20: Qualitative counterfactual results generated by LD-ViCE on the FERV39k dataset, transforming the predicted class emotion *Neutral* into each of the other emotion classes. The generated counterfactuals exhibit distinct and class-consistent facial dynamics corresponding to the desired emotional categories.



Figure 21: Qualitative counterfactual results generated by LD-ViCE on the FERV39k dataset, transforming the predicted class emotion *Sad* into each of the other emotion classes. The generated counterfactuals exhibit distinct and class-consistent facial dynamics corresponding to the desired emotional categories.



Figure 22: Qualitative counterfactual results generated by LD-ViCE on the FERV39k dataset, transforming the predicted class emotion *Sad* into each of the other emotion classes. The generated counterfactuals exhibit distinct and class-consistent facial dynamics corresponding to the desired emotional categories.

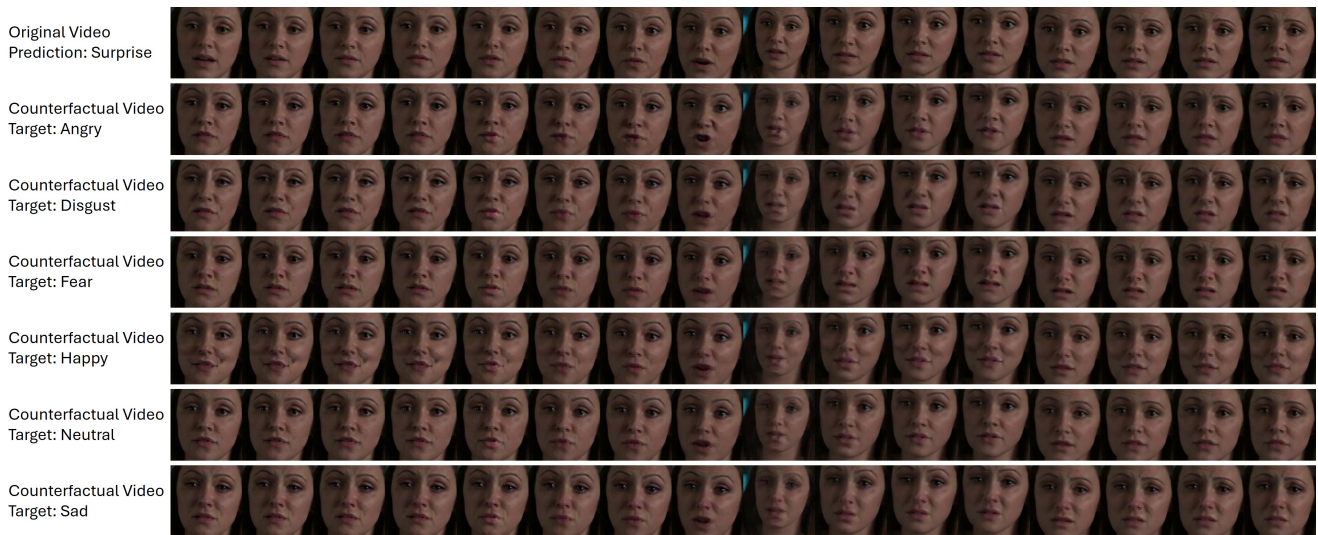


Figure 23: Qualitative counterfactual results generated by LD-ViCE on the FERV39k dataset, transforming the predicted class emotion *Surprise* into each of the other emotion classes. The generated counterfactuals exhibit distinct and class-consistent facial dynamics corresponding to the desired emotional categories.

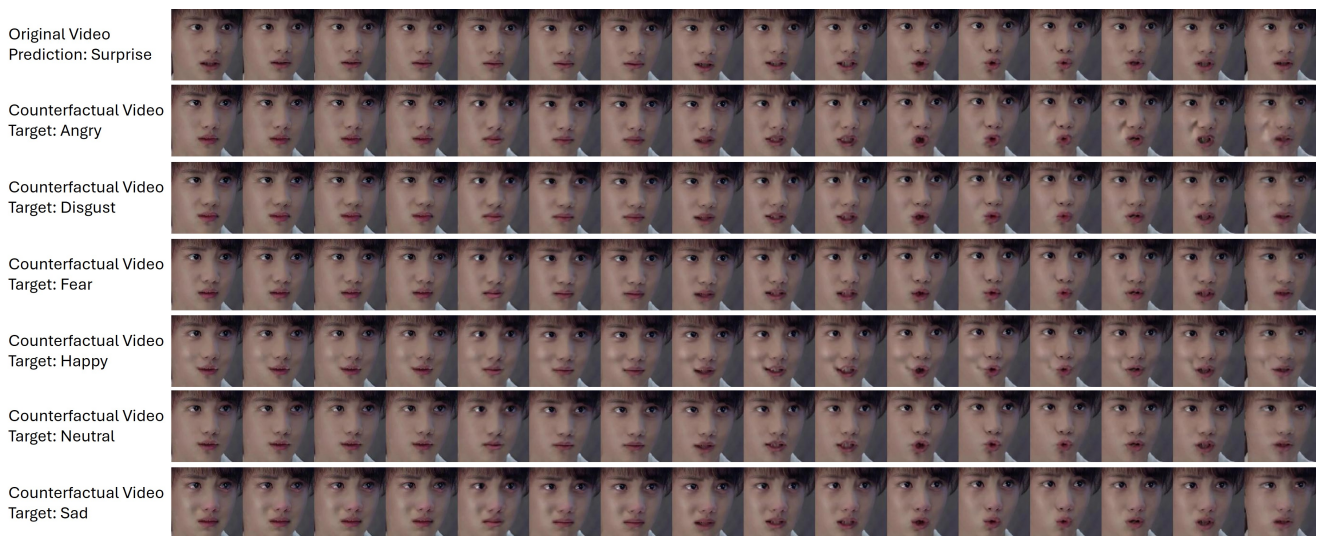


Figure 24: Qualitative counterfactual results generated by LD-ViCE on the FERV39k dataset, transforming the predicted class emotion *Surprise* into each of the other emotion classes. The generated counterfactuals exhibit distinct and class-consistent facial dynamics corresponding to the desired emotional categories.

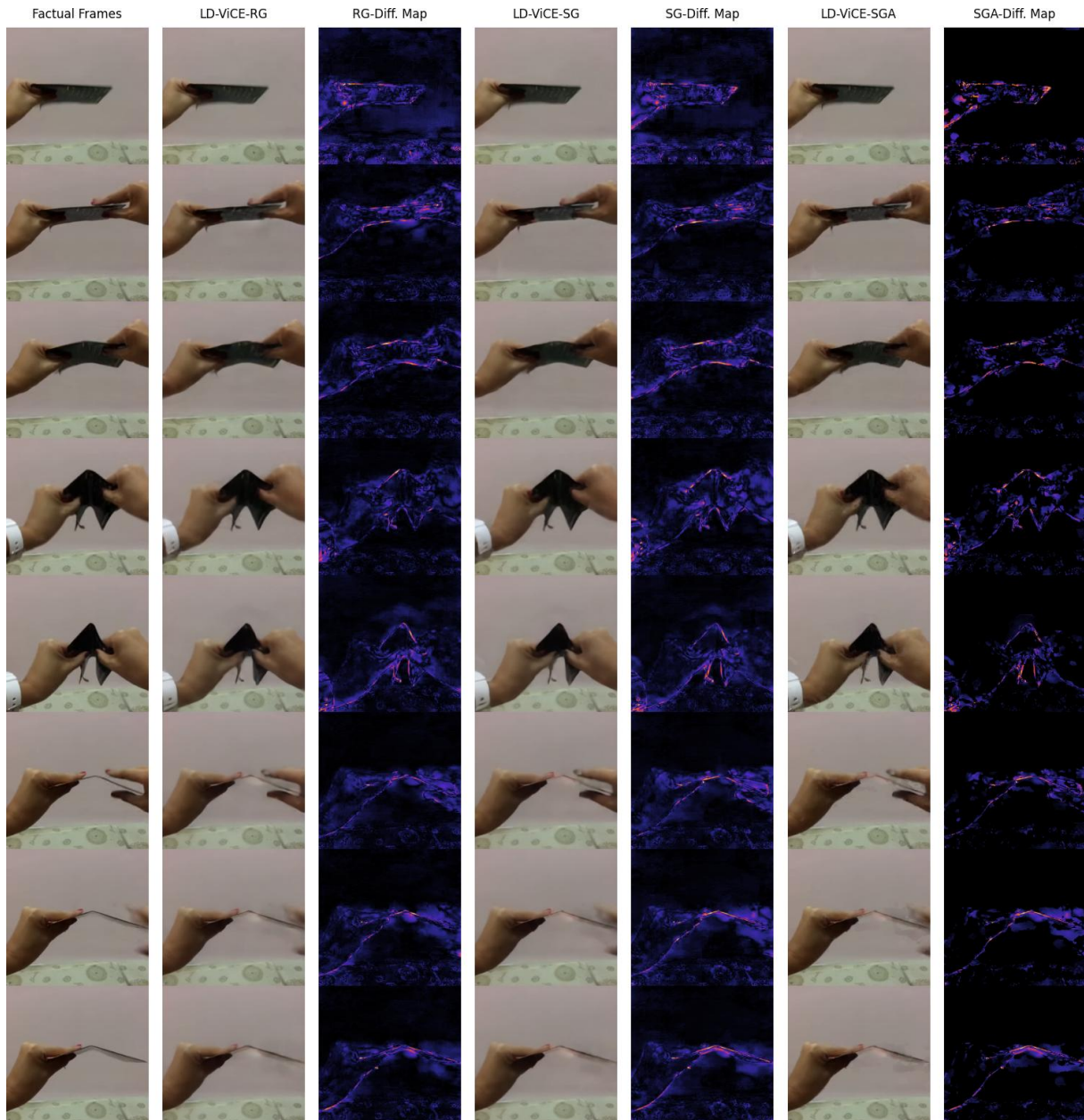


Figure 25: Qualitative counterfactual results for transforming the predicted action from *Bending something so that it deforms* to *Bending something until it breaks* on the SSv2 dataset, using LD-ViCE variants RG, SG, and SGA with corresponding difference maps. The SGA variant produces the most spatially localized changes. Changes are primarily applied to the expected interaction region, and in the final frames, a visible break appears in the manipulated object.

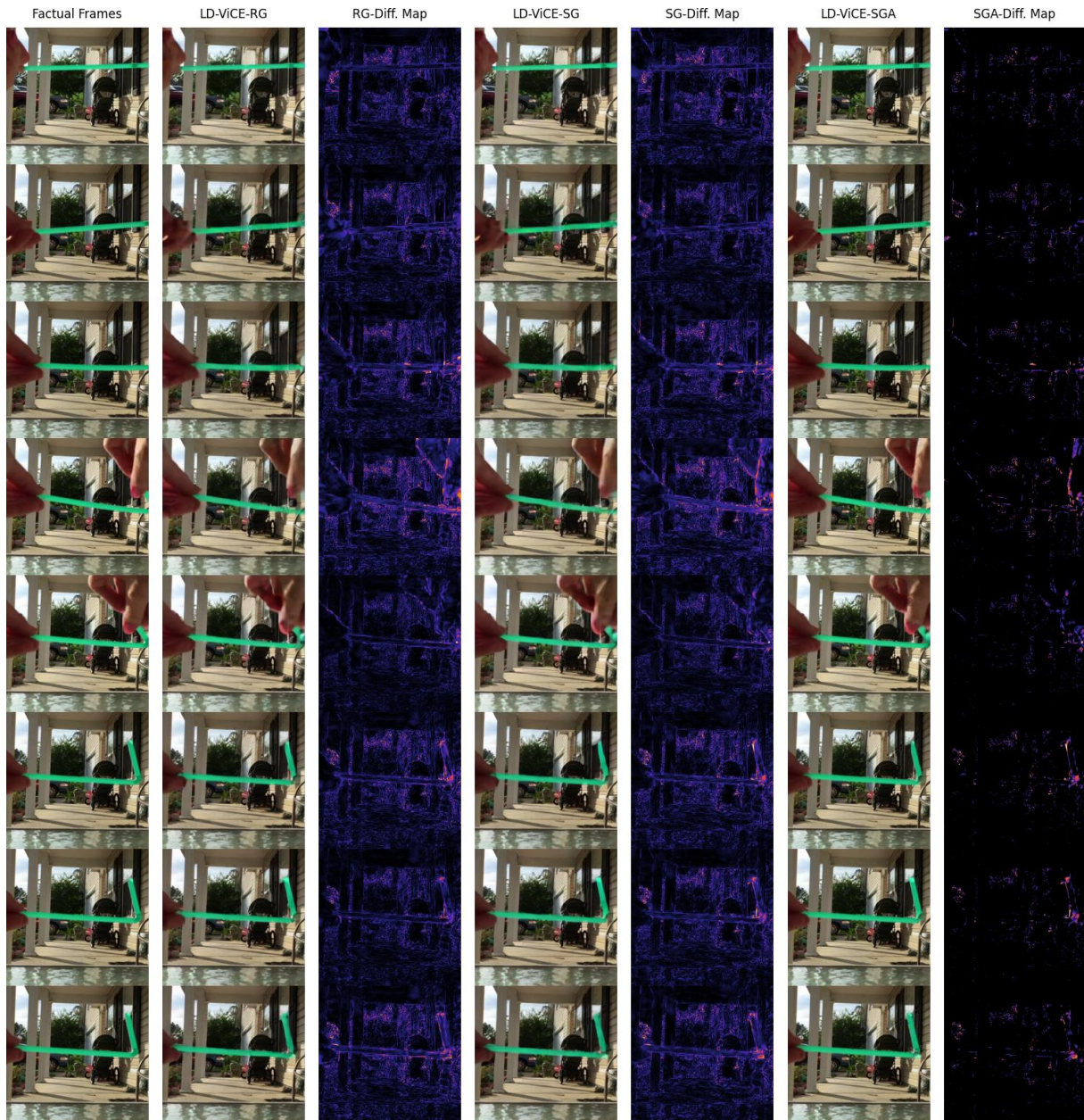


Figure 26: Qualitative counterfactual results for transforming the predicted action from *Bending something so that it deforms* to *Bending something until it breaks* on the SSv2 dataset, using LD-ViCE variants RG, SG, and SGA with corresponding difference maps. The SGA variant produces the most spatially localized changes. Modifications are concentrated in the expected interaction region, and in the final frames, a visible break emerges in the middle of the straw.

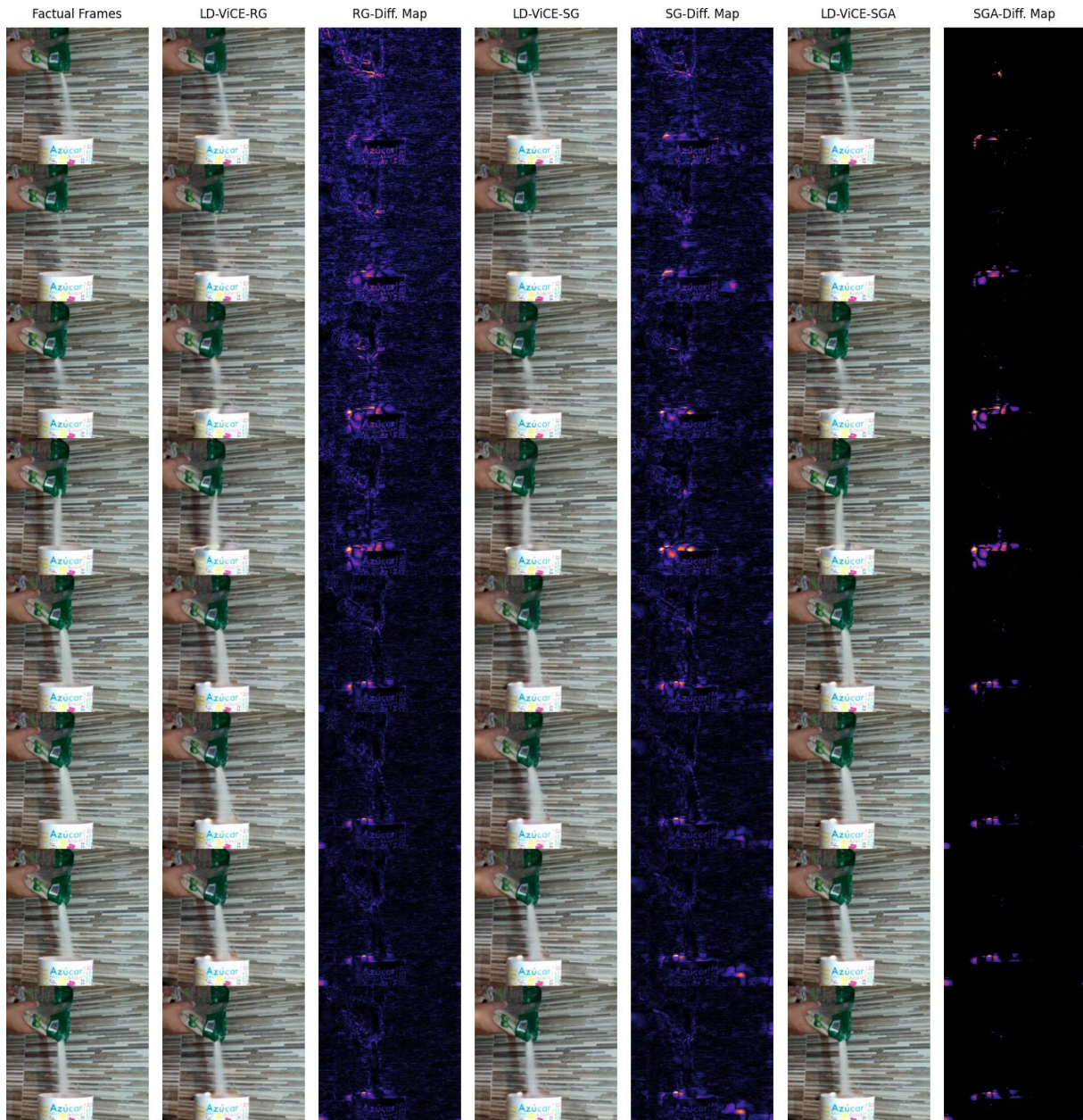


Figure 27: Qualitative counterfactual results for transforming the predicted action from *Pouring something into something* to *Pouring something into something until it overflows* on the SSv2 dataset, using LD-ViCE variants RG, SG, and SGA with corresponding difference maps. The SGA variant localizes changes more effectively than RG or SG. Modifications occur near the pouring region, creating the effect of a filled container without clear visual evidence of overflowing liquid.



Figure 28: Qualitative counterfactual results for transforming the predicted action from *Pouring something into something* to *Pouring something into something until it overflows* on the SSv2 dataset, using LD-ViCE variants RG, SG, and SGA with corresponding difference maps. Modifications occur near the pouring region, creating the effect of a filled container without clear visual evidence of overflowing liquid. The SGA variant localizes changes more effectively than RG or SG.